A Radiomics-based Machine Learning Approach for Identification of Ischemic Cardiomyopathy in Oxygenation-Sensitive Cardiovascular Magnetic Resonance Images

Nikoo Mashayekhi

Division of Experimental Medicine

Faculty of Medicine and Health Sciences, McGill University, Montreal

April 2024

A thesis submitted to McGill University in partial fulfillment of the requirements of the degree of Master of Science

Table of Contents

Abbreviation Glossary

CMR : Cardiovascular Magnetic Resonance

MRI : Magnetic Resonance Imaging

ICMP : Ischemic Cardiomyopathy

CAD : Coronary Artery Disease

MI : Myocardial Infarction

OS-CMR : Oxygenation-Sensitive Cardiovascular Magnetic Resonance Imaging

LGE: Late Gadolinium Enhancement

CT : Computed Tomography

BOLD : blood oxygen level dependent

RF: Radio Frequency

SSFP: Steady-State Free Precession

bSSFP: Balanced Steady-State Free Precession

CNN: Convolutional Neural Networks

ROI : Region of Interest

LOG : Laplacian of Gaussian

GLCM : Gray Level Co-occurrence Matrix

GLRLM : Gray Level Run Length Matrix

GLSZM : Gray Level Size Zone Matrix

NGTDM : Neighboring Gray Tone Difference Matrix

GLDM : Gray Level Dependence Matrix

ROC : Receiver operating characteristic

Abstract- English

Ischemic cardiomyopathy (ICMP) is a condition where heart muscle damage due to decreased blood flow, or ischemia, impairs the heart's ability to pump blood efficiently. On a tissue level, severe irreversible ischemic injury, also known as myocardial infarction (MI), results in a fibrotic scar. Cardiovascular Magnetic Resonance (CMR) imaging is a valuable tool for the quantitative assessment of the heart's morphology and function, but its unique ability lies in the ability to provide information on tissue pathology such as viualizing the extent of myocardial infarction and differentiate damaged myocardium from healthy and viable tissue. However, conventional CMR approaches require the acquisition of multiple images using multiple acquisition protocols and several slices, which is time-consuming. Most importantly, CMR imaging of myocardial scars necessitates an intravenous application of contrast agents, posing risks to patients with renal impairment and increasing the complexity of the imaging procedure.

Oxygenation-sensitive Cardiovascular Magnetic Resonance (OS-CMR) is a novel, experimentally validated approach that uses the Blood Oxygen Level Dependent (BOLD) effect, where deoxygenated hemoglobin acts as a natural contrast agent in the magnetic field. This technique can be combined with vasoactive breathing maneuvers—paced hyperventilation followed by a breath hold—to visualize changes in myocardial oxygenation that can be induced by vasoactive medication on by breathing maneuvers. The breathing maneuvers induce carbon dioxide variations, causing vasoconstriction during hyperventilation and vasodilation during a long breath-hold. This method thus provides a means to assess abnormalities of the vascular function in affected ischemic or infarcted regions without the need for external contrast agents.

Radiomics refers to the extraction of a large number of quantitative features from medical images using advanced computational algorithms. When paired with Artificial Intelligence

(AI), radiomics transforms these features into valuable clinical information that can predict disease characteristics and outcomes. The integration of radiomics with AI algorithms holds the potential to enhance patient-specific predictions by learning complex patterns in the data that may be imperceptible to the human eye.

This study aims to explore the potential of combining OS-CMR with radiomics and AI techniques to identify ICMP. By using a four-minute, non-contrast, and detailed imaging OS-CMR protocol and the analytical power of radiomics, this study aims to develop a robust, non-invasive diagnostic approach for identifying patients with ICMP.

Abstract- Français

La cardiomyopathie ischémique (ICMP) est une condition dans laquelle des lésions du muscle cardiaque dues à une diminution du flux sanguin, ou ischémie, altèrent la capacité du cœur à pomper le sang de manière efficace. À l'échelle tissulaire, une lésion ischémique sévère et irréversible, également connue sous le nom d'infarctus du myocarde (MI), aboutit à une cicatrice fibreuse. L'imagerie par résonance magnétique cardiovasculaire (CMR) est un outil précieux pour l'évaluation quantitative de la morphologie et de la fonction cardiaques, mais sa capacité unique réside dans la possibilité de fournir des informations sur la pathologie tissulaire, telles que la visualisation de l'étendue de l'infarctus du myocarde et la différenciation entre le myocarde endommagé et le tissu sain et viable. Cependant, les approches conventionnelles de la CMR nécessitent l'acquisition de plusieurs images en utilisant divers protocoles d'acquisition et plusieurs coupes, ce qui prend du temps. Plus important encore, l'imagerie par CMR des cicatrices myocardiques nécessite l'application intraveineuse d'agents de contraste, ce qui pose des risques pour les patients souffrant d'insuffisance rénale et augmente la complexité de la procédure d'imagerie.

L'imagerie par résonance magnétique cardiovasculaire sensible à l'oxygénation (OS-CMR) est une approche novatrice, validée expérimentalement, qui utilise l'effet de dépendance au niveau d'oxygène sanguin (BOLD), où l'hémoglobine désoxygénée agit comme un agent de contraste naturel dans le champ magnétique. Cette technique peut être combinée avec des manœuvres respiratoires vasoactives—hyperventilation rythmée suivie d'une apnée—pour visualiser les changements de l'oxygénation myocardique pouvant être induits par des médicaments vasoactifs ou par des manœuvres respiratoires. Les manœuvres respiratoires induisent des variations du dioxyde de carbone, provoquant une vasoconstriction pendant l'hyperventilation et une vasodilatation pendant une apnée prolongée. Cette méthode offre ainsi un moyen

d'évaluer les anomalies de la fonction vasculaire dans les régions ischémiques ou infarctées touchées, sans nécessiter d'agents de contraste externes.

Le radiomique fait référence à l'extraction d'un grand nombre de caractéristiques quantitatives à partir d'images médicales à l'aide d'algorithmes computationnels avancés. Associé à l'intelligence artificielle (AI), le radiomique transforme ces caractéristiques en informations cliniques précieuses qui peuvent prédire les caractéristiques et les résultats de la maladie. L'intégration du radiomique avec des algorithmes d'AI offre le potentiel d'améliorer les prédictions spécifiques aux patients en apprenant des motifs complexes dans les données qui peuvent être imperceptibles à l'œil humain.

Cette étude vise à explorer le potentiel de la combinaison de l'OS-CMR avec les techniques de radiomique et d'AI pour identifier l'ICMP. En utilisant un protocole d'imagerie OS-CMR détaillé, non contrasté, de quatre minutes, et la puissance analytique du radiomique, cette étude vise à développer une approche diagnostique robuste et non invasive pour identifier les patients atteints d'ICMP.

Acknowledgments

I would like to extend my deepest gratitude to the many individuals who have contributed to the completion of this thesis. First and foremost, I am grateful to Dr. Matthias Friedrich for his unwavering support and inspiration throughout this journey. His dynamic lab environment, insightful feedback, and consistent motivation have been crucial to my development as a researcher. I also sincerely thank Dr. Mitchel Benovoy, whose technical expertise has significantly enhanced my skills and understanding. I am thankful for the opportunities he provided that allowed me to grow technically and professionally and for his trust in my capabilities. I am equally thankful to Dr. Michael Chetrit, whose creative ideas and ongoing encouragement have greatly aided my research progress. His ability to motivate and support me consistently has been invaluable. I owe a special thank you to Dr. Judy Luu, who introduced me to the clinical aspects of cardiovascular MRI. Her engaging teaching sessions and thorough mentoring have laid a solid foundation for my understanding and interest in this field.

Additionally, I extend my appreciation to the entire team at the Courtois Cardiovascular Magnetic Resonance Research Group at the McGill University Health Centre. Special thanks to Margherita Leo and Sylvie Gelineau, the technologists whose expertise in imaging was indispensable for the acquisition of all the images used in this research. I am also grateful to Dr. Javad Rafiee for his insightful comments and profound medical knowledge.

My gratitude extends to Kathleen Amedee and Adonis Rodaros for their administrative support, ensuring that all processes ran smoothly. I'm also thankful for the support from my fellow students—Katerina Eyre, Mayssa Moukarzel, Kate Lindsay, Arseniy Kokotov, Faezeh Lotfi Kazemi, Shadi Abdolrahimi, and Marcus Saldanha. Your friendship was invaluable as I adjusted to life in this new city, and I am grateful for the moments we shared. A special thanks to Kate Lindsay for her invaluable help with my thesis writing, providing essential resources, guidance, and meticulous editing.

I owe a particular debt of gratitude to my parents and my brother, whose unwavering belief in me has been a constant source of strength. Despite the distance, your support has been immense, inspiring me to pursue my dreams with determination. I am profoundly grateful for your love and encouragement.

Thesis Overview

This thesis is structured into three chapters, each aimed at advancing the understanding and application of oxygenation-sensitive cardiovascular magnetic resonance (OS-CMR) combined with medical imaging radiomics for the diagnosis of ischemic cardiomyopathy (ICMP).

Chapter 1 provides the background context by delineating the significance of OS-CMR as a contrast-free method for evaluating myocardial oxygenation non-invasively. It highlights the utility of OS-CMR in diagnosing heart diseases, particularly myocardial ischemia, and introduces medical imaging radiomics as an emerging field using quantitative features extracted from images to automate disease assessment. The chapter outlines the study's objective to assess the potential of radiomic features extracted from OS-CMR images in identifying cases of ischemic cardiomyopathy.

Chapter 2 presents an original research manuscript, describing the automatic segmentation of the myocardium, data analysis, and the extraction of radiomic features from short-axis images captured across various phases of the cardiac cycle. Feature selection and a Random Forest classifier for distinguishing between healthy and ischemic cardiomyopathy cases are also explained.

Chapter 3 The chapter addresses the potential of combining radiomic feature extraction from OS-CMR cine images with machine learning techniques for efficient and non-invasive stratification of heart conditions in clinical settings.

Contribution of Authors

Chapter 1: Nikoo Mashayekhi (NM) was the primary writer and editor of the chapter. Dr. Michael Chetrit (MC) and Kate Lindsay (KL) contributed by editing the text after the first draft was completed by NM. Dr. Matthias Friedrich (MF) then contributed by editing the final version.

Chapter 2: This original research manuscript is being prepared for future submission and publication with NM as the first author. NM was the primary writer and editor of the chapter. NM was involved in writing the study protocols for ethics submission, study design, model development and statistical analysis, interpretation of data, figure and table creation, as well as writing, and editing of the manuscript. Arseniy Kokotov and Faezeh Lotfi Kazemi contributed by also writing the study protocols for ethics submission. Elisavet Konidis contributed by revising study protocols for ethics submission after the draft was completed. Dr. Mitchel Benovoy contributed to the design of the methodology of the study. MC was involved in the conceptual design of the study and editing of the manuscript after the first draft was completed by NM. Dr. Judy Luu contributed by providing scientific guidance and helpful suggestions.

Chapter 3: NM was the primary writer and editor of the chapter. KL contributed by editing the text after the first draft was completed by NM. MF contributed by editing the final version.

List of Figures

List of Tables

1 Chapter 1: Introduction and Literature Review

1.1 Introduction

Ischemic cardiomyopathy (ICMP), characterized by impaired myocardial function due to reduced blood flow and a subsequent decrease in oxygen and nutrient supply with ischemic tissue damage, is a leading cause of death worldwide [1]. This condition can lead to adverse cardiac events, including heart failure and sudden cardiac death [2]. Traditionally, the definitive diagnosis of ICMP has relied on procedures such as coronary angiography, computed tomography (CT) angiogram, late gadolinium enhanced (LGE) imaging, and adenosine stress testing, each of which has its limitations and risks for patients[3].

Oxygenation-sensitive cardiovascular magnetic resonance imaging (OS-CMR) is a novel non-invasive technique to assess cardiovascular function by capitalizing on the unique behaviour of deoxygenated hemoglobin, which, due to its paramagnetic nature, serves as an endogenous contrast agent within the magnetic field, such that of an MRI scanner, influencing signal strength in response to its concentration changes [4]. This phenomenon, recognized as the blood oxygen level-dependent (BOLD) effect, helps reveal changes in tissue oxygenation across different regions. Changes in OS-CMR signal intensities can be expressed as the inducible relative increase in signal intensity, called the myocardial oxygenation reserve (MORE), which quantifies the responsiveness of the coronary vascular system tracking the oxygenation-related signal intensity levels during vasoactive maneuvers such as vasodilation infusion or a breathing maneuver against those at rest [5]. It has been observed that patient populations with coronary artery disease (CAD) or those at risk for the disease typically show a reduced MORE compared to healthy controls [6]. This capacity of OS-CMR to track oxygenation changes provides potentially valuable information for the non-invasive diagnosis of ICMP.

Radiomics is a technique that involves the extraction of a potentially large number of quantitative features from medical images, which aid in characterizing shape and texture of the tissue in these images and transforming them into mineable high-dimensional data. Research has demonstrated the potential clinical utility of radiomics in CMR. For instance, a study by Baessler et al. [7] highlighted the potential of CMR texture analysis to distinguish between hypertrophic cardiomyopathy (HCM) and normal hearts using non-contrast cine images. Similarly, a study by Cetin et al. [8] showed that radiomics could detect subtle myocardial architecture changes, which might not be apparent through conventional image inspection, offering a novel perspective in assessing hypertension-induced myocardial alterations. Furthermore, the application of radiomics extends to differentiating between various disease states, providing incremental accuracy in identifying conditions such as HCM from hypertensive heart disease, and also discerning acute from chronic myocardial infarctions with a high degree of precision [9], [10]. These examples substantiate the utility of radiomics in refining cardiovascular disease identification, understanding myocardial pathology, and potentially predicting clinical outcomes. When paired with artificial intelligence (AI) methodologies, radiomic features can be used to develop predictive models capable of automatically identifying cardiac diseases.

Given the promising capabilities of radiomics and AI in CMR, this study aims to use these techniques to explore the potential of OS-CMR imaging in identifying ischemic cardiomyopathy.

1.2 Cardiovascular Magnetic Resonance

Cardiovascular magnetic resonance (CMR) is a non-invasive imaging modality that uses magnetic resonance imaging (MRI) to assess the function and structure of the cardiovascular system and is particularly valued for its ability to provide high-resolution images without

ionizing radiation [11]. This section provides an overview of CMR, its principles, and its applications in clinical practice.

1.2.1 Principles of Magnetic Resonance Imaging

The fundamental principles of MRI revolve around the magnetic properties of atomic nuclei. When placed in a strong magnetic field, the nuclei of atoms with a polarity and thus a magnetic moment align with the field. In the human body, the most abundant of such atoms are hydrogen atoms (protons) [12]. In the magnetic field, protons also show a specific movement called precession, also referred to as 'spin'. Because this movement has a known frequency, an external application of a pulse with that frequency can induce a resonant. For the MR experiment, a resonant radio frequency (RF) pulse is applied that lifts protons to a higher energy level, also disrupting the alignment. When the pulse is turned off, the nuclei return to their original equilibrium state, releasing a detectable amount of energy [12]. Antennas (coils) and the MRI scanner capture this emitted energy and use it to create detailed images. This energy is translated into a greyscale value (signal) in the images. Because the signal intensity varies in intensity depending on the type of tissue and its chemical environment, its display allows for the differentiation between tissue characteristics [13].

The terms describing the duration of the relaxation process after the pulse are T1 relaxation (longitudinal) and T2 relaxation (transverse). These relaxation times provide valuable information about tissue characteristics and different pathologies. T1 relaxation reflects the recovery of longitudinal magnetization of the nuclei back to equilibrium along the direction of the magnetic field [14]. Tissues with shorter T1 relaxation times typically appear bright on T1-weighted images, while those with longer T1 relaxation times appear darker. This is particularly evident in pathologies where T1 values are elevated due to increased interstitial space, such as in amyloid deposition or fibrosis [14]. In contrast, T2 relaxation represents the

loss of coherence in the spins of the nuclei following excitation, occurring perpendicular to the direction of the static magnetic field. Tissues with shorter T2 relaxation times appear dark on T2-weighted images, while those with longer T2 relaxation times appear bright. For instance, tissues with high water content, such as edema or inflammation, often display prolonged T2 relaxation times, with an increased signal intensity on T2-weighted images. This is particularly useful in diagnosing acute conditions such as myocarditis and acute myocardial infarction [15].

1.2.2 Utility of Cardiovascular Magnetic Resonance

CMR distinguishes itself from cardiac CT, coronary angiography, and nuclear imaging, which rely on ionizing radiation, by deriving tissue contrast from the intrinsic physical properties of tissues itself. It covers the assessment of morphology, contractile function, and blood flow within a single examination. This comprehensive capability enables CMR to diagnose a wide array of heart conditions, including myocardial ischemia, cardiomyopathies, myocarditis, vascular diseases, and congenital heart diseases. [16]. Regarded as the gold standard method for measuring the volumes of the left and right ventricles, CMR is crucial for identifying and understanding different types of cardiomyopathies.

Late gadolinium enhancement (LGE) in CMR is a technique that uses the behavior of gadolinium-based contrast agents within the heart's extracellular space to highlight differences in tissue composition [17]. The principle behind LGE is the differential shortening of the T1 relaxation time caused by these contrast agents, which accumulate differently in normal and diseased myocardial tissues due to variations in their uptake and elimination [18]. Clinically, LGE is invaluable in detecting and characterizing a range of myocardial diseases, from myocardial infarction and myocarditis to cardiomyopathies including ICMP, by identifying areas of scar tissue, fibrosis, and other myocardial injuries [18]. However, it has been observed that the use of gadolinium-based contrast agents in CMR can lead to gadolinium deposition in

the brain and other tissues [19]. It can also cause complications for patients with renal impairments, highlighting the need for imaging methods that do not rely on contrast agents, which would be especially beneficial for these patient populations [20].

1.2.3 Principles of Oxygenation-Sensitive Cardiovascular Magnetic Resonance

Oxygenation-Sensitive Cardiovascular Magnetic Resonance (OS-CMR), is a diagnostic imaging technique used to evaluate oxygenation changes within myocardial tissue [21]. This method is particularly valuable because it offers a non-invasive way to assess myocardial oxygenation by detecting mismatches in oxygen supply and demand [5]. It can highlight inhomogneities and regions with an abnormal vascular response and subsequent variations of the oxygenation-sensitive signal intensity.

OS-CMR uses the Blood Oxygen Level-dependent (BOLD) effect, which is primarily based on the magnetic properties of deoxygenated hemoglobin. Deoxygenated hemoglobin is a paramagnetic molecule that reduces local magnetic field homogeneity, which can be visualized as a reduction in signal intensity [22]. In contrast, oxygenated hemoglobin acts as a weakly diamagnetic molecule and therefore slightly increases local magnetic field homogeneity, causing a signal intensity increase in OS images. These changes, particularly evident in tissues with significant variations in deoxygenated hemoglobin concentration, accelerate the decay of transverse (T2) relaxation, impacting signal intensity [5]. T2* signal, which is a subset of T2, predominates in heterogeneous tissues and reflects the rate of magnetic resonance signal decay over time. It is influenced by the presence of deoxygenated hemoglobin, thereby affecting the BOLD signal in tissues with a more rapidly decaying transverse relaxation. In cases of ischemia i.e. regional relative myocardial deoxygenation, the concentration of deoxygenated hemoglobin in capillary blood increases, resulting in T2* shortening and consequently decreased signal intensity on OS-CMR images [5]. The contrasting effects of oxygenated and

deoxygenated hemoglobin on the local magnetic field of MRI serve as an intrinsic contrast agent [23]. This phenomenon shows the utility of OS-CMR in identifying regions of reduced oxygenation within the myocardium. Areas that show normal increases and decreases in blood flow during breathing maneuvers are considered normal, whereas areas that do not vary much are deemed abnormal or ischemic. This is particularly beneficial for diagnosing conditions such as CAD and ICMP, where localized oxygen deficits may occur. OS-CMR distinguishes itself by its capacity to map and monitor changes in myocardial oxygenation without necessitating contrast agents.

Breathing maneuvers, involving controlled hyperventilation followed by a maximal breath-hold, have emerged as a viable and less invasive alternative to traditional pharmaceutical vasodilators like adenosine for assessing vascular function in cardiovascular imaging. Historically, adenosine has been used in OS-CMR to detect regional blood flow deficits across various patient populations [24]. Despite its efficacy, the use of adenosine is often limited by contraindications and adverse effects [25]. In contrast, carbon dioxide (CO2), a potent endogenous vasodilator, has been explored for its ability to induce vasodilation more safely [26]. Although CO2 and other vasoactive stimuli can reveal endothelial dysfunction through attenuated vasodilatory responses, practical limitations such as patient compliance and issues with signal-to-noise ratio (SNR) have curtailed their widespread use [27].

Breathing maneuvers have been validated in several studies as a suitable substitute for inhaled CO2, showcasing their applicability in diverse patient groups [28], [29], [30]. These maneuvers induce measurable myocardial oxygenation changes detectable by OS-CMR, providing information about myocardial blood flow and vascular resistance [31]. Specifically, hyperventilation-induced hypocapnia leads to vasoconstriction and an increase in vascular resistance, reducing OS-CMR signal intensity due to a relative increase in deoxyhemoglobin. Conversely, breath-hold-induced hypercapnia results in vasodilation and decreased vascular

resistance, increasing OS-CMR signal intensity [31]. Further research has demonstrated that breathing maneuvers not only increase patient comfort but also potentially offer greater sensitivity to myocardial oxygenation changes compared to adenosine, with fewer adverse effects [32]. They have also been effective in detecting inducible ischemia in animal models and multivessel CAD patients, as well as in highlighting microvascular dysfunction in conditions like obstructive sleep apnea, heart failure, and post-heart transplantation [28], [29], [33], [34], [35], [36].

1.3 Ischemic Cardiomyopathy

Ischemic cardiomyopathy (ICMP) refers to a condition where the heart's ability to pump blood efficiently is reduced due to damage (infarction) or chronic severe ischemia [37]. This term is closely linked with coronary artery disease (CAD), which is characterized by the buildup of plaques in the coronary arteries, leading to decreased oxygen and nutrient supply to the heart muscle [38]. Initially, there's a reversible decline in the heart's contraction ability due to decreased oxygen supply. However, prolonged ischemia causes irreversible myocardial damage, known as myocardial infarction (MI) [39]. Various factors contribute to the development of ICMP, including CAD, coronary plaque rupture, coronary vasculitis, coronary artery dissection, coronary microvascular disease, and fibromuscular dysplasia to name a few [40]. Risk factors for heart disease, such as having a family history of cardiovascular disease, high blood pressure, tobacco use, diabetes, high cholesterol, obesity, and physical inactivity, can increase the risk of developing ICMP [37].

This section provides an overview of diagnostic approaches of ICMP and the role of CMR in diagnosing and assessing the severity of ICMP.

1.3.1 Diagnostic Approaches and Challenges

Common clinical methods used to assess patients suspected of ICMP include echocardiography, Single-Photon Emission Computed Tomography (SPECT), Positron Emission Tomography (PET), Computed Tomography (CT), X-ray coronary angiography, and CMR [41]. Each of these methods has its strengths and limitations.

Echocardiography is a widely available real-time imaging modality and is suitable for initial evaluation of ischemia. However, its image quality can be influenced by patient factors such as obesity or lung disease, as well as the operator's experience, and seldom can one comment on the presence of ischemic injury or scar [42]. SPECT imaging in conjunction with a vasodilator provides functional assessment for detecting perfusion defects indicative of ischemia, but it involves radiation exposure and has limited spatial resolution compared to other modalities [43]. Stress-PET imaging offers high sensitivity and specificity in detecting myocardial perfusion abnormalities but is less widely available, and also involves exposure to radioactive material [44]. CT angiography provides detailed anatomical information about coronary arteries and can detect coronary artery stenosis. However, it traditionally lacked the ability to determine if the stenosis was causing myocardial ischemia [45]. Recent advancements, such as CT fractional flow reserve (FFR), artificial intelligence, and perfusion imaging, now allow for the assessment of ischemia [46], [47]. However, this method still requires contrast administration and exposes both patients and physicians to radiation. Coronary angiography remains the gold standard to assess for luminal narrowing due to its high spatial resolution, and the intravascular assessment of plaque is the current gold standard for the assessment of ischemia. However, this technique comes at the cost of its invasive nature in addition to the radiation exposure [48].

CMR addresses the common limitations of the aforementioned imaging techniques by providing high resolution images non-invasively and without ionizing radiation, and is a promising approach to identify the presence of ischemia and to assess the severity of ICMP. The following section provides more details about how CMR is used in cases of suspected ICMP.

1.3.2 Cardiovascular Magnetic Resonance in Identification of Ischemic Cardiomyopathy

When investigating ICMP, CMR stress perfusion tests are confirmed to be a valuable, accurate tool for providing information about the distribution and severity of myocardial perfusion deficits [49]. This method typically uses pharmaceutical vasodilators such as adenosine to induce stress conditions that amplify myocardial blood flow differences between healthy and ischemic tissues. Alongside, gadolinium-based contrast agents are injected to enhance the visualization of myocardial perfusion during the first pass of the contrast through the heart. The resultant images provide detailed insights into areas where blood flow is compromised. [50]. The resulting first-pass perfusion images are then analyzed to estimate the blood flow efficiency in the heart. CMR has proven useful in CAD [51]. However, its utility is limited by its reliance on substances that may pose risks to certain patient groups. Pharmaceutical vasodilators can provoke adverse reactions such as chest discomfort, headache, and more severe cardiovascular effects, particularly in patients with severe asthma or chronic obstructive pulmonary disease (COPD) due to their potential to significantly alter respiratory and cardiac function [52]. They also create challenges regarding logistics, added preparation time, and cost. Gadolinium-based contrast agents, while generally safe for most patients, are associated with a small yet relevant risk of nephrogenic systemic fibrosis, a rare but serious condition primarily affecting patients with severe renal impairment [53]. Additionally, it has been observed that

the use of gadolinium-based contrast agents in CMR can lead to gadolinium deposition in the brain and other tissues, which raises concerns about potential long-term effects [19]. These agents can also cause mild to moderate allergic reactions, which necessitates caution in patients with a history of allergic responses to contrast materials [54].

1.4 Radiomics

Radiomics is a field in medical imaging that uses advanced processing techniques to extract voxel-level quantitative features characterizing global and regional photometric, geometrical, and textural properties of medical images [55]. The main idea of radiomics is to transform medical images into high-dimensional, mineable data by extracting numerical features characterizing patterns and information that may not be visible to the human eye [56]. These extracted features can then serve as biomarkers and be integrated with statistical and machine learning models to enhance the prediction and diagnosis of different diseases [56].

Radiomics was initially applied in oncology and has demonstrated remarkable success in that area. Several studies have proved the utility of radiomics in characterizing tumor phenotypes. For instance, radiomic texture analysis of prostate MRI has shown the utility for differentiating non-cancerous tissue from prostate cancer and for distinguishing different prostate cancer grades [57]. It has demonstrated considerable potential in predicting treatment responses. In a study conducted by Ahmed et al., texture analysis was found to be highly effective in predicting response to chemotherapy in breast cancer patients, revealing significant differences in texture parameters between responders and partial responders [58]. Similarly, it has been shown that radiomic data from CT scans of primary tumors and lymph nodes can accurately predict how patients with advanced lung cancer respond to treatment before surgery [59]. Additionally, radiomics has shown promise in prognostication. It has been shown that a CT-based radiomic signature can accurately predict distant metastasis in patients with lung adenocarcinoma,

providing valuable prognostic information beyond traditional clinical factors [60]. The extensive work done in oncology suggests that analyzing image phenotype through radiomics texture analysis could provide valuable information into tissue-level pathology [61].

These radiomic features can be extracted from the selected region of interest (ROI) in original images or preprocessed images obtained through various filtering techniques including Laplacian of Gaussian (LoG) filtering and wavelet decomposition. LOG filtering applies a Gaussian blur to the original image, followed by edge detection using the Laplacian operator, and can be performed at different scales (sigmas) to capture features at different levels of detail [62]. Wavelet transform decomposes the 3D images into different frequency components using high and low pass filters that selectively capture high or low frequencies. These components include LLH (low-low-high), HHL (high-high-low), HHH (high-high-high) filters, and so forth, enabling multi-resolution feature extraction [63].

Radiomic features can be categorized into first-order, shape, and texture features, including Gray-Level Co-Occurrence Matrix (GLCM), Gray-Level Dependence Matrix (GLDM), Neighborhood Gray-Tone Difference Matrix (NGTDM), Gray-Level Run Length Matrix (GLRLM), and Gray-Level Size Zone Matrix (GLSZM), which will be elaborated subsequently [64]. Appendix A provides the complete description of imaging features used in this work.

First Order: First-order features describe basic statistical properties of pixel intensities within a ROI in an image, without considering spatial relationships between pixels. These features include commonly calculated statistics such as mean, median, standard deviation, skewness, kurtosis, and entropy. First-order features provide information about the distribution and variation of voxel intensities in an image.

Shape: Shape features characterize the geometric properties of the ROI, such as size, volume, surface area, and compactness.

Gray-Level Co-Occurrence Matrix (GLCM): quantifies the spatial relationships between pairs of pixel intensities within an image. It calculates the frequency of occurrence of pixel intensity pairs at specified spatial offsets and directions. From the GLCM, various texture features can be derived, including contrast, correlation, energy, and homogeneity, which capture different aspects of texture complexity and spatial patterns within the image [65].

Gray-Level Dependence Matrix (GLDM): GLDM measures the dependence between pixel pairs based on their gray-level values and spatial relationships. It characterizes the frequency of occurrence of different gray-level pairs within an image, along with their corresponding spatial distances. GLDM features, such as contrast, dissimilarity, and homogeneity, quantify the variability and regularity of gray-level transitions within the image.

Neighborhood Gray-Tone Difference Matrix (NGTDM): NGTDM assesses the differences in gray-level values between a central pixel and its surrounding neighbors within a specified neighborhood. It quantifies the variability of gray-level differences in different directions and distances, and provides information about the local texture and contrast variations within the image.

Gray-Level Run Length Matrix (GLRLM): GLRLM captures the distribution of continuous runs of consecutive pixels with the same gray-level value in different directions within an image. It calculates the lengths and frequencies of these runs, from which features such as short run emphasis, long run emphasis, and run length non-uniformity can be derived. GLRLM features characterize the texture and spatial continuity of homogeneous regions within the image [66].

Gray-Level Size Zone Matrix (GLSZM): GLSZM quantifies the distribution of connected regions with homogeneous gray-level values of varying sizes within an image. It characterizes the spatial distribution and sizes of these homogeneous zones, and provides information about the heterogeneity and coarseness of textures present in the ROI.

1.4.1 Radiomics in Cardiovascular Magnetic Resonance

Numerous studies have demonstrated the utility of using CMR radiomics for texture analysis. A subset of these studies has concentrated on deriving comparable information from non-contrast images to those obtained through gadolinium-based images, with the ultimate aim of avoiding the need for contrast. For instance, Avard et al. explored the effectiveness of radiomics features extracted from non-contrast cine images, alongside machine learning algorithms, for MI detection [67]. Their study, involving 72 patients, revealed that radiomics analysis enabled accurate differentiation between MI and normal tissue, achieving an optimal performance, suggesting its potential as an alternative diagnostic method to LGE [67]. In another study, Fahmy et al. presented a model using radiomic features derived from balanced steady state free precession (bSSFP) cine images to identify hypertrophic cardiomyopathy (HCM) patients without scar to potentially spare them from unnecessary gadolinium administration [68].

CMR radiomics studies have also aimed to extract textural features from LGE images. Amano et al. conducted research focusing on patients with HCM and demonstrated differences in textural features extracted from LGE images between individuals with and without a history of ventricular tachycardia [69]. This finding shows the utility of radiomics in identifying subtle variations associated with arrhythmic events in HCM patients. Similarly, Kotu et al. investigated the predictive value of textural features derived from LGE scar in 34 individuals with chronic MI [70]. Their study revealed that these features offer incremental prognostic

value beyond scar size and location, particularly in assessing the risk of life-threatening arrhythmias. Additionally, Cheng et al. explored the association between LGE textural features and adverse clinical outcomes in individuals with HCM and reduced left ventricular systolic function [71]. And found a robust correlation between radiomic features of LGE images and an endpoint including death and life-threatening arrhythmias.

These studies illustrate the potential of CMR radiomics to enhance current methods of image analysis and provide accurate disease classification and prognostic estimation without the need for injected contrast.

1.5 Artificial Intelligence

Artificial intelligence (AI) refers to the development of computer systems capable of mimicking cognitive functions, such as recognizing patterns and making decisions [72]. AI algorithms learn from data, identify patterns, and make predictions based on them. With its rapidly growing significance in medicine [73], [74], specifically in the field of medical imaging, AI is likely to revolutionize clinical practice in the coming years [75].

Machine Learning (ML) is a subset of AI. In classical ML methods, a model, which is a function that makes predictions based on input data, is trained using a predefined set of features [76]. These features, selected and extracted from the data, are what the model uses to learn and make predictions. One of the most advanced ML techniques, Deep Learning (DL), takes a different approach by employing neural networks, inspired by the structure of the human brain, to automatically discover the relevant features directly from the data [77]. This section will provide an overview of AI applications in CMR, followed by an explanation of some key AI concepts used in the original research manuscript.

1.5.1 Artificial Intelligence in Cardiovascular Magnetic Resonance

AI applications in CMR are diverse and extensive. Key applications include optimization of image acquisition and reconstruction, automated segmentation of the left and right ventricle, myocardial tissue characterization, diagnosis, and prognosis. The following is a brief literature review of each of these applications:

Image Acquisition and Reconstruction:

One of the primary challenges in CMR is the lengthy acquisition times, due to the respiratory and cardiac motion [78]. AI, particularly DL models have shown promise in improving speed and quality of image acquisition and reconstruction. These DL-based approaches focus on two key objectives: to shorten the image acquisition time and increase the overall efficiency of the imaging process and enhance the quality of the images by mitigating artifacts and reducing noise. Muscogiuri et al. employed DL to reduce noise in LGE images, enhancing image clarity without compromising diagnostic quality [79]. Schemper et al. and Lebet et al. introduced Convolutional Neural Network (CNN) based approaches for automatic reconstruction and quality improvement in CMR imaging, showcasing the potential for AI to automate complex processing tasks [80], [81]. Furthermore, studies by Frick et al., Yokoyama et al., Nitta et al., and Lu et al. demonstrated ML's capability in automating view and slice alignment, reducing the manual effort required in CMR imaging [82], [83], [84], [85].

Image Segmentation:

In CMR post-processing, the delineation of heart chambers and myocardium, known as segmentation, is essential but is traditionally a manual and time-intensive process. Despite the high precision achieved by experienced readers, the variability among them and the amount of time it takes remains a challenge [86]. Recognizing this, a substantial volume of research has aimed at automating CMR segmentation to improve efficiency and precision [87], [88],

although manual interventions are often still necessary for complex regions. DL methods have been effectively applied to myocardial and cardiac chamber segmentation from CMR images, frequently employing pixel-based classification strategies. Notably, the U-Net architecture has been widely used for this purpose [89], with various studies employing basic CNN layouts for segmenting short-axis CMR images [90]. Additionally, researchers like Bai et al. have innovated by incorporating contextual 3D spatial information within CNN architectures, enhancing the segmentation's accuracy [91]. Other innovations in DL segmentation involve boundary regression techniques for contour generation rather than pixel classification [92], [93].

Myocardial Tissue Characterization, Diagnosis, and Prognosis:

In section 1.4.1 the application of radiomics in characterizing myocardial tissue was discussed. These radiomic features can be used as data points to train AI models for diagnosing heart conditions. Furthermore, CMR imaging not only aids in diagnosis but also in prognosis, as demonstrated by a meta-analysis by El Aidi et al., which identified key predictors of cardiovascular events [94]. Machine learning enhances this by analyzing vast patient data, including CMR findings, for more accurate outcome predictions, as shown in the study by Ambale-Venkatesh et al. [95].

1.5.2 Machine Learning-Based Classification

Machine Learning (ML) is a subset of AI that focuses on developing algorithms and statistical models that enable computers to perform specific tasks without using explicit instructions [96]. Instead, these systems learn and make predictions or decisions based on data. Machine learning is broadly categorized into supervised and unsupervised learning, each serving different purposes based on the structure of the data available [96].

Supervised learning is one of the most common types of machine learning, where the model is trained on a labelled dataset [97]. This means that for each piece of data in the training set, the

outcome or label is already known. The goal of supervised learning is to train the model so well that when it is given new data, it can predict the correct output based on what it has learned from the training set. This approach is widely used in applications where the prediction of future events or classification of data into predefined categories is required. Unsupervised learning, on the other hand, deals with data that does not have labelled responses. The system tries to learn the patterns and the structure from the data without any guidance on what the outcome should be. It is used for clustering, association, and dimensionality reduction tasks where the goal is to explore the underlying structure of the data [97].

Classification, a type of supervised learning, involves categorizing data into predefined classes or groups. It is one of the most significant tasks in machine learning and has extensive applications in various fields, including image recognition, and medical diagnosis [98]. The essence of classification is to build a model on a training dataset, where the classes are known, and then use this model to classify new, unseen data into these classes. Radiomic features can serve as a valuable training set for classification tasks due to their ability to capture detailed information from medical images. These features can provide rich data representations that facilitate the differentiation between various classes, making them useful for training machine learning models [99].

Several classification models exist, each suited for different tasks and datasets. The choice of model depends on factors such as the nature of the data, and the complexity of the classification problem [100]. Some commonly used classification models include decision trees, support vector machines, logistic regression, and random forests [96]. Each of these models has its strengths and weaknesses. In this study, random forests had superior performance and achieved the best results among all classification models tested. The next section explains this machine learning model.

1.5.2.1 Random Forest

Random Forest is a widely used supervised machine learning algorithm frequently used for classification tasks. Its core comprises multiple decision trees, each representing a hierarchical structure that organizes data based on input features [101]. In a decision tree, at each node, a decision is made regarding which branch to follow based on the value of a specific feature [102]. This process continues recursively until reaching the terminal nodes (leaf nodes), where final predictions are made. What distinguishes Random Forest is its ensemble approach, where a multitude of decision trees are generated [101]. Each tree is trained on a random subset of the available data and a random subset of features. This randomness injects diversity into the individual trees, making the overall model more robust. Subsequently, the predictions of these trees are combined through averaging, to produce the final outcome. This ensemble strategy helps Random Forest to mitigate overfitting and enhance generalization [101].

1.5.3 Feature Selection

Feature selection is a preprocessing step in developing machine learning models. It involves the identification and selection of a subset of relevant features from the original set of features in a dataset. Its primary aim is to enhance model performance, reduce computational complexity, and improve interpretability by focusing only on the most informative and discriminative features [103].

In the context of radiomics, where we have a large number of quantitative features, feature selection becomes very important due to the high dimensionality of the feature space [104]. Not all these radiomics features are equally informative or relevant for predictive modelling tasks. Many of these features may be redundant, noisy, or irrelevant to the underlying pathology or clinical outcomes of interest. Therefore, effective feature selection techniques are needed for identifying and retaining only the most discriminative and informative radiomic features,

to enhance model performance, reduce overfitting, and improve the interpretability of machine learning models [104].

1.5.3.1 Boruta Algorithm

The Boruta algorithm is an advanced feature selection method designed to identify the most relevant features in a dataset for predictive modelling, especially useful in scenarios where we have labelled data and the goal is to select features that vary significantly between classes [105]. Originating from the Random Forest classification technique, Boruta works by creating randomized copies (shadows) of all features in the dataset and then iteratively comparing the importance of real features against these shadows. This process helps in determining the relevance of each feature by evaluating if they stand out in terms of importance when compared to the baseline set by the shadow features. The algorithm continues this evaluation until all features are either confirmed as significant or rejected as irrelevant, ensuring that the model includes only those variables that have a meaningful impact on distinguishing between different classes. This selection process enhances the accuracy and effectiveness of predictive models by focusing on the most informative features [105].

1.6 Summary

In this chapter, the utility of CMR imaging was examined, focusing on its role in diagnosing and assessing ICMP. The fundamental principles of MRI were explained, along with the applications of CMR in clinical practice. Specifically, the significance of OS-CMR in providing non-invasive insights into myocardial oxygenation status was presented, offering valuable diagnostic information without the need for invasive procedures or contrast agents.

Furthermore, radiomics and its application in cardiovascular imaging was discussed, highlighting the potential of radiomic features extracted from OS-CMR images to augment diagnostic accuracy. Additionally, the integration of AI techniques, particularly machine learning algorithms, in cardiac imaging was explored. Feature selection methodologies were also discussed, emphasizing the efficacy of techniques like the Boruta algorithm in identifying salient imaging features for diagnostic modeling.

Overall, this chapter provided a comprehensive overview of OS-CMR imaging, radiomics, and AI in the diagnosis of ICMP.

1.7 References

[1] M. A. Khan *et al.*, “Global Epidemiology of Ischemic Heart Disease: Results from the Global Burden of Disease Study,” *Cureus*, vol. 12, no. 7, p. e9349, doi: 10.7759/cureus.9349.

[2] C. Gräni, D. C. Benz, S. Gupta, S. Windecker, and R. Y. Kwong, “Sudden Cardiac Death in Ischemic Heart Disease: From Imaging Arrhythmogenic Substrate to Guiding Therapies,” *JACC Cardiovasc. Imaging*, vol. 13, no. 10, pp. 2223–2238, Oct. 2020, doi: 10.1016/j.jcmg.2019.10.021.

[3] M. Tavakol, S. Ashraf, and S. J. Brener, “Risks and Complications of Coronary Angiography: A Comprehensive Review,” *Glob. J. Health Sci.*, vol. 4, no. 1, pp. 65–93, Jan. 2012, doi: 10.5539/gjhs.v4n1p65.

[4] C. M. Wacker *et al.*, “Changes in myocardial oxygenation and perfusion under pharmacological stress with dipyridamole: assessment using T*2 and T1 measurements,” *Magn. Reson. Med.*, vol. 41, no. 4, pp. 686–695, Apr. 1999, doi: 10.1002/(sici)1522-2594(199904)41:4<686::aid-mrm6>3.0.co;2-9.

[5] M. G. Friedrich and T. D. Karamitsos, “Oxygenation-sensitive cardiovascular magnetic resonance,” *J. Cardiovasc. Magn. Reson.*, vol. 15, no. 1, p. 43, May 2013, doi: 10.1186/1532-429X-15-43.

[6] J. M. Luu, A. Schmidt, J. Flewitt, Y. Mikami, H. Ter Keurs, and M. G. Friedrich, “Cardiovascular risk is associated with a transmural gradient of myocardial oxygenation during adenosine infusion,” *Eur. Heart J. Cardiovasc. Imaging*, vol. 20, no. 11, pp. 1287–1295, Nov. 2019, doi: 10.1093/ehjci/jey202.

[7] B. Baeßler, M. Mannil, D. Maintz, H. Alkadhi, and R. Manka, “Texture analysis and machine learning of non-contrast T1-weighted MR images in patients with hypertrophic cardiomyopathy-Preliminary results,” *Eur. J. Radiol.*, vol. 102, pp. 61–67, May 2018, doi: 10.1016/j.ejrad.2018.03.013.

[8] I. Cetin, S. E. Petersen, S. Napel, O. Camara, M. A. G. Ballester, and K. Lekadir, “A radiomics approach to analyze cardiac alterations in hypertension,” in *2019 IEEE 16th International Symposium on Biomedical Imaging (ISBI 2019)*, Apr. 2019, pp. 640–643. doi: 10.1109/ISBI.2019.8759440.

[9] U. Neisius, H. El-Rewaidy, S. Nakamori, J. Rodriguez, W. J. Manning, and R. Nezafat, “Radiomic Analysis of Myocardial Native T1 Imaging Discriminates Between Hypertensive Heart Disease and Hypertrophic Cardiomyopathy,” *JACC Cardiovasc. Imaging*, vol. 12, no. 10, pp. 1946–1954, Oct. 2019, doi: 10.1016/j.jcmg.2018.11.024.

[10] B. Baessler, M. Mannil, S. Oebel, D. Maintz, H. Alkadhi, and R. Manka, “Subacute and Chronic Left Ventricular Myocardial Scar: Accuracy of Texture Analysis on Nonenhanced Cine MR Images,” *Radiology*, vol. 286, no. 1, pp. 103–112, Jan. 2018, doi: 10.1148/radiol.2017170213.

[11] D. C. Lee *et al.*, “The growth and evolution of cardiovascular magnetic resonance: a 20-year history of the Society for Cardiovascular Magnetic Resonance (SCMR) annual scientific sessions,” *J. Cardiovasc. Magn. Reson.*, vol. 20, p. 8, Jan. 2018, doi: 10.1186/s12968-018-0429-z.

[12] “An Introduction to Magnetic Resonance Imaging: From Image Acquisition to Clinical Diagnosis | Request PDF.” Accessed: Mar. 26, 2024. [Online]. Available: https://www.researchgate.net/publication/226073222_An_Introduction_to_Magnetic_Resonance_Imaging_From_Image_Acquisition_to_Clinical_Diagnosis

[13] T. A. Gallagher, A. J. Nemeth, and L. Hacein-Bey, “An introduction to the Fourier transform: relationship to MRI,” *AJR Am. J. Roentgenol.*, vol. 190, no. 5, pp. 1396–1405, May 2008, doi: 10.2214/AJR.07.2874.

[14] R. J. Perea *et al.*, “T1 mapping: characterisation of myocardial interstitial space,” *Insights Imaging*, vol. 6, no. 2, pp. 189–202, Nov. 2014, doi: 10.1007/s13244-014-0366-9.

[15] R. Wassmuth *et al.*, “Variability and homogeneity of cardiovascular magnetic resonance myocardial T2-mapping in volunteers compared to patients with edema,” *J. Cardiovasc. Magn. Reson.*, vol. 15, no. 1, p. 27, Mar. 2013, doi: 10.1186/1532-429X-15-27.

[16] F. von Knobelsdorff-Brenkenhoff and J. Schulz-Menger, “Role of cardiovascular magnetic resonance in the guidelines of the European Society of Cardiology,” *J. Cardiovasc. Magn. Reson.*, vol. 18, p. 6, Jan. 2016, doi: 10.1186/s12968-016-0225-6.

[17] “The histologic basis of late gadolinium enhancement cardiovascular magnetic resonance in hypertrophic cardiomyopathy | Journal of the American College of

Cardiology.” Accessed: Apr. 13, 2024. [Online]. Available: https://www.jacc.org/doi/abs/10.1016/j.jacc.2004.03.035

[18] H. Satoh *et al.*, “Distribution of late gadolinium enhancement in various types of cardiomyopathies: Significance in differential diagnosis, clinical features and prognosis,” *World J. Cardiol.*, vol. 6, no. 7, pp. 585–601, Jul. 2014, doi: 10.4330/wjc.v6.i7.585.

[19] B. J. Guo, Z. L. Yang, and L. J. Zhang, “Gadolinium Deposition in Brain: Current Scientific Evidence and Future Perspectives,” *Front. Mol. Neurosci.*, vol. 11, p. 335, Sep. 2018, doi: 10.3389/fnmol.2018.00335.

[20] F. Martino, G. Amici, M. Rosner, C. Ronco, and G. Novara, “Gadolinium-Based Contrast Media Nephrotoxicity in Kidney Impairment: The Physio-Pathological Conditions for the Perfect Murder,” *J. Clin. Med.*, vol. 10, no. 2, p. 271, Jan. 2021, doi: 10.3390/jcm10020271.

[21] E. Hillier, J. Covone, and M. G. Friedrich, “Oxygenation-sensitive Cardiac MRI with Vasoactive Breathing Maneuvers for the Non-invasive Assessment of Coronary Microvascular Dysfunction,” *J. Vis. Exp. JoVE*, no. 186, Aug. 2022, doi: 10.3791/64149.

[22] M. G. Friedrich, T. Niendorf, J. Schulz-Menger, C. M. Gross, and R. Dietz, “Blood oxygen level-dependent magnetic resonance imaging in patients with stress-induced angina,” *Circulation*, vol. 108, no. 18, pp. 2219–2223, Nov. 2003, doi: 10.1161/01.CIR.0000095271.08248.EA.

[23] D. P. Guensch *et al.*, “The blood oxygen level dependent (BOLD) effect of in-vitro myoglobin and hemoglobin,” *Sci. Rep.*, vol. 11, p. 11464, Jun. 2021, doi: 10.1038/s41598-021-90908-x.

[24] U. Ikeda, K. Kurosaki, K. Ohya, and K. Shimada, “Adenosine stimulates nitric oxide synthesis in vascular smooth muscle cells,” *Cardiovasc. Res.*, vol. 35, no. 1, pp. 168–174, Jul. 1997, doi: 10.1016/s0008-6363(97)00068-0.

[25] T. Voigtländer *et al.*, “The adverse events and hemodynamic effects of adenosine-based cardiac MRI,” *Korean J. Radiol.*, vol. 12, no. 4, pp. 424–430, 2011, doi: 10.3348/kjr.2011.12.4.424.

[26] J. E. Brian, “Carbon dioxide and the cerebral circulation,” *Anesthesiology*, vol. 88, no. 5, pp. 1365–1386, May 1998, doi: 10.1097/00000542-199805000-00029.

[27] F. C. Moreton, K. A. Dani, C. Goutcher, K. O’Hare, and K. W. Muir, “Respiratory challenge MRI: Practical aspects,” *NeuroImage Clin.*, vol. 11, pp. 667–677, May 2016, doi: 10.1016/j.nicl.2016.05.003.

[28] K. Fischer *et al.*, “Feasibility of cardiovascular magnetic resonance to detect oxygenation deficits in patients with multi-vessel coronary artery disease triggered by breathing maneuvers,” *J. Cardiovasc. Magn. Reson. Off. J. Soc. Cardiovasc. Magn. Reson.*, vol. 20, no. 1, p. 31, May 2018, doi: 10.1186/s12968-018-0446-y.

[29] F. Roubille, K. Fischer, D. P. Guensch, J.-C. Tardif, and M. G. Friedrich, “Impact of hyperventilation and apnea on myocardial oxygenation in patients with obstructive sleep apnea - An oxygenation-sensitive CMR study,” *J. Cardiol.*, vol. 69, no. 2, pp. 489–494, Feb. 2017, doi: 10.1016/j.jjcc.2016.03.011.

[30] M. Elharram *et al.*, “Regional Heterogeneity in the Coronary Vascular Response in Women With Chest Pain and Nonobstructive Coronary Artery Disease,” *Circulation*, vol. 143, no. 7, pp. 764–766, Feb. 2021, doi: 10.1161/CIRCULATIONAHA.120.052520.

[31] D. P. Guensch, K. Fischer, J. A. Flewitt, and M. G. Friedrich, “Impact of intermittent apnea on myocardial tissue oxygenation--a study using oxygenation-sensitive cardiovascular magnetic resonance,” *PloS One*, vol. 8, no. 1, p. e53282, 2013, doi: 10.1371/journal.pone.0053282.

[32] K. Fischer, D. P. Guensch, and M. G. Friedrich, “Response of myocardial oxygenation to breathing manoeuvres and adenosine infusion,” *Eur. Heart J. Cardiovasc. Imaging*, vol. 16, no. 4, pp. 395–401, Apr. 2015, doi: 10.1093/ehjci/jeu202.

[33] E. Hillier, T. Hafyane, and M. Friedrich, “285Myocardial and cerebral oxygenation deficits in heart failure patients - a multi-parametric study,” *Eur. Heart J. - Cardiovasc. Imaging*, vol. 20, Jun. 2019, doi: 10.1093/ehjci/jez114.003.

[34] N. Iannino, K. Fischer, M. Friedrich, T. Hafyane, F.-P. Mongeon, and M. White, “Myocardial Vascular Function Assessed by Dynamic Oxygenation-sensitive Cardiac Magnetic Resonance Imaging Long-term Following Cardiac Transplantation,” *Transplantation*, vol. 105, no. 6, pp. 1347–1355, Jun. 2021, doi: 10.1097/TP.0000000000003419.

[35] K. Fischer, D. P. Guensch, N. Shie, J. Lebel, and M. G. Friedrich, “Breathing Maneuvers as a Vasoactive Stimulus for Detecting Inducible Myocardial Ischemia - An Experimental Cardiovascular Magnetic Resonance Study,” *PloS One*, vol. 11, no. 10, p. e0164524, 2016, doi: 10.1371/journal.pone.0164524.

[36] K. Fischer *et al.*, “Insights Into Myocardial Oxygenation and Cardiovascular Magnetic Resonance Tissue Biomarkers in Heart Failure With Preserved Ejection Fraction,” *Circ. Heart Fail.*, vol. 15, no. 4, p. e008903, Apr. 2022, doi: 10.1161/CIRCHEARTFAILURE.121.008903.

[37] B. Bhandari, B. S. Quintanilla Rodriguez, and W. Masood, “Ischemic Cardiomyopathy,” in *StatPearls*, Treasure Island (FL): StatPearls Publishing, 2024. Accessed: Mar. 08, 2024. [Online]. Available: http://www.ncbi.nlm.nih.gov/books/NBK537301/

[38] P. A. McCullough, “Coronary Artery Disease,” *Clin. J. Am. Soc. Nephrol.*, vol. 2, no. 3, p. 611, May 2007, doi: 10.2215/CJN.03871106.

[39] “Cell Biology of Ischemia/Reperfusion Injury - PMC.” Accessed: Apr. 13, 2024. [Online]. Available: https://www.ncbi.nlm.nih.gov/pmc/articles/PMC3904795/

[40] “Ischemic Cardiomyopathy: What You Need To Know,” Cleveland Clinic. Accessed: Mar. 30, 2024. [Online]. Available: https://my.clevelandclinic.org/health/diseases/17145-ischemic-cardiomyopathy

[41] C. Doesch and T. Papavassiliu, “Diagnosis and management of ischemic cardiomyopathy: Role of cardiovascular magnetic resonance imaging,” *World J. Cardiol.*, vol. 6, no. 11, pp. 1166–1174, Nov. 2014, doi: 10.4330/wjc.v6.i11.1166.

[42] J. Soongswang *et al.*, “Limitation of transthoracic echocardiography in the diagnosis of congenital heart diseases,” *J. Med. Assoc. Thail. Chotmaihet Thangphaet*, vol. 83 Suppl 2, pp. S111-117, Nov. 2000.

[43] M. Egred, G. D. Waiter, T. W. Redpath, S. K. I. Semple, A. Al-Mohammad, and S. Walton, “Blood oxygen level-dependent (BOLD) MRI: A novel technique for the assessment of myocardial ischemia as identified by nuclear imaging SPECT,” *Eur. J. Intern. Med.*, vol. 18, no. 8, pp. 581–586, Dec. 2007, doi: 10.1016/j.ejim.2007.03.013.

[44] P. A. Kaufmann and P. G. Camici, “Myocardial blood flow measurement by PET: technical aspects and clinical applications,” *J. Nucl. Med. Off. Publ. Soc. Nucl. Med.*, vol. 46, no. 1, pp. 75–88, Jan. 2005.

[45] Z. Sun, G. H. Choo, and K. H. Ng, “Coronary CT angiography: current status and continuing challenges,” *Br. J. Radiol.*, vol. 85, no. 1013, pp. 495–510, May 2012, doi: 10.1259/bjr/15296170.

[46] Y. Tanabe *et al.*, “Computed tomographic evaluation of myocardial ischemia,” *Jpn. J. Radiol.*, vol. 38, no. 5, pp. 411–433, 2020, doi: 10.1007/s11604-020-00922-8.

[47] N. S. Nurmohamed *et al.*, “Development and Validation of a Quantitative Coronary CT Angiography Model for Diagnosis of Vessel-Specific Coronary Ischemia,” *JACC Cardiovasc. Imaging*, vol. 17, no. 8, pp. 894–906, Aug. 2024, doi: 10.1016/j.jcmg.2024.01.007.

[48] E. J. Topol and S. E. Nissen, “Our preoccupation with coronary luminology. The dissociation between clinical and angiographic findings in ischemic heart disease,” *Circulation*, vol. 92, no. 8, pp. 2333–2342, Oct. 1995, doi: 10.1161/01.cir.92.8.2333.

[49] A. Scatteia and S. Dellegrottaglie, “Cardiac magnetic resonance in ischemic cardiomyopathy: present role and future directions,” *Eur. Heart J. Suppl.*, vol. 25, no. Supplement_C, pp. C58–C62, May 2023, doi: 10.1093/eurheartjsupp/suad007.

[50] T. Kotecha *et al.*, “Automated Pixel-Wise Quantitative Myocardial Perfusion Mapping by CMR to Detect Obstructive Coronary Artery Disease and Coronary Microvascular Dysfunction: Validation Against Invasive Coronary Physiology,” *JACC Cardiovasc. Imaging*, vol. 12, no. 10, pp. 1958–1969, Oct. 2019, doi: 10.1016/j.jcmg.2018.12.022.

[51] “Assessment of stable coronary artery disease by cardiovascular magnetic resonance imaging: Current and emerging techniques - PMC.” Accessed: Apr. 14, 2024. [Online]. Available: https://www.ncbi.nlm.nih.gov/pmc/articles/PMC5329750/

[52] H. M. Lak, S. Ranka, and A. Goyal, “Pharmacologic Stress Testing,” in *StatPearls*, Treasure Island (FL): StatPearls Publishing, 2024. Accessed: Apr. 14, 2024. [Online]. Available: http://www.ncbi.nlm.nih.gov/books/NBK555963/

[53] Y. M. Shamam and O. De Jesus, “Nephrogenic Systemic Fibrosis,” in *StatPearls*, Treasure Island (FL): StatPearls Publishing, 2024. Accessed: Apr. 14, 2024. [Online]. Available: http://www.ncbi.nlm.nih.gov/books/NBK567754/

[54] M. O. Baerlocher, M. Asch, and A. Myers, “Allergic-type reactions to radiographic contrast media,” *CMAJ Can. Med. Assoc. J.*, vol. 182, no. 12, p. 1328, Sep. 2010, doi: 10.1503/cmaj.090371.

[55] V. Kumar *et al.*, “Radiomics: the process and the challenges,” *Magn. Reson. Imaging*, vol. 30, no. 9, pp. 1234–1248, Nov. 2012, doi: 10.1016/j.mri.2012.06.010.

[56] “Radiomics: Images Are More than Pictures, They Are Data | Radiology.” Accessed: Feb. 13, 2024. [Online]. Available: https://pubs.rsna.org/doi/full/10.1148/radiol.2015151169

[57] A. Wibmer *et al.*, “Haralick texture analysis of prostate MRI: utility for differentiating non-cancerous prostate from prostate cancer and differentiating prostate cancers with different Gleason scores,” *Eur. Radiol.*, vol. 25, no. 10, pp. 2840–2850, Oct. 2015, doi: 10.1007/s00330-015-3701-8.

[58] A. Ahmed, P. Gibbs, M. Pickles, and L. Turnbull, “Texture analysis in assessment and prediction of chemotherapy response in breast cancer,” *J. Magn. Reson. Imaging JMRI*, vol. 38, no. 1, pp. 89–101, Jul. 2013, doi: 10.1002/jmri.23971.

[59] T. P. Coroller *et al.*, “Radiomic-Based Pathological Response Prediction from Primary Tumors and Lymph Nodes in NSCLC,” *J. Thorac. Oncol. Off. Publ. Int. Assoc. Study Lung Cancer*, vol. 12, no. 3, pp. 467–476, Mar. 2017, doi: 10.1016/j.jtho.2016.11.2226.

[60] T. P. Coroller *et al.*, “CT-based radiomic signature predicts distant metastasis in lung adenocarcinoma,” *Radiother. Oncol. J. Eur. Soc. Ther. Radiol. Oncol.*, vol. 114, no. 3, pp. 345–350, Mar. 2015, doi: 10.1016/j.radonc.2015.02.015.

[61] “Decoding tumour phenotype by noninvasive imaging using a quantitative radiomics approach - PubMed.” Accessed: Mar. 30, 2024. [Online]. Available: https://pubmed.ncbi.nlm.nih.gov/24892406/

[62] C. S. Brenner, “B Y D. MARR A N D E. HILDRETH”.

[63] R. S. Pathak, *THE WAVELET TRANSFORM*. Springer Science & Business Media, 2009.

[64] “Computational Radiomics System to Decode the Radiographic Phenotype - PubMed.” Accessed: Mar. 23, 2024. [Online]. Available: https://pubmed.ncbi.nlm.nih.gov/29092951/

[65] P. Lambin *et al.*, “Radiomics: the bridge between medical imaging and personalized medicine,” *Nat. Rev. Clin. Oncol.*, vol. 14, no. 12, pp. 749–762, Dec. 2017, doi: 10.1038/nrclinonc.2017.141.

[66] G. Thibault, J. Angulo, and F. Meyer, “Advanced statistical matrices for texture characterization: application to cell classification,” *IEEE Trans. Biomed. Eng.*, vol. 61, no. 3, pp. 630–637, Mar. 2014, doi: 10.1109/TBME.2013.2284600.

[67] E. Avard *et al.*, “Non-contrast Cine Cardiac Magnetic Resonance image radiomics features and machine learning algorithms for myocardial infarction detection,” *Comput. Biol. Med.*, vol. 141, p. 105145, Feb. 2022, doi: 10.1016/j.compbiomed.2021.105145.

[68] A. S. Fahmy, E. J. Rowin, A. Arafati, T. Al-Otaibi, M. S. Maron, and R. Nezafat, “Radiomics and deep learning for myocardial scar screening in hypertrophic cardiomyopathy,” *J. Cardiovasc. Magn. Reson.*, vol. 24, no. 1, p. 40, Jun. 2022, doi: 10.1186/s12968-022-00869-x.

[69] Y. Amano, Y. Suzuki, F. Yanagisawa, Y. Omori, and N. Matsumoto, “Relationship between Extension or Texture Features of Late Gadolinium Enhancement and Ventricular Tachyarrhythmias in Hypertrophic Cardiomyopathy,” *BioMed Res. Int.*, vol. 2018, p. 4092469, Sep. 2018, doi: 10.1155/2018/4092469.

[70] “Cardiac magnetic resonance image-based classification of the risk of arrhythmias in post-myocardial infarction patients - PubMed.” Accessed: Mar. 30, 2024. [Online]. Available: https://pubmed.ncbi.nlm.nih.gov/26239472/

[71] “LGE-CMR-derived texture features reflect poor prognosis in hypertrophic cardiomyopathy patients with systolic dysfunction: preliminary results - PubMed.” Accessed: Mar. 30, 2024. [Online]. Available: https://pubmed.ncbi.nlm.nih.gov/29728817/

[72] S. Russell and J. Bohannon, “Artificial intelligence. Fears of an AI pioneer,” *Science*, vol. 349, no. 6245, p. 252, Jul. 2015, doi: 10.1126/science.349.6245.252.

[73] C. Krittanawong, H. Zhang, Z. Wang, M. Aydar, and T. Kitai, “Artificial Intelligence in Precision Cardiovascular Medicine,” *J. Am. Coll. Cardiol.*, vol. 69, no. 21, pp. 2657–2664, May 2017, doi: 10.1016/j.jacc.2017.03.571.

[74] K. W. Johnson *et al.*, “Artificial Intelligence in Cardiology,” *J. Am. Coll. Cardiol.*, vol. 71, no. 23, pp. 2668–2679, Jun. 2018, doi: 10.1016/j.jacc.2018.03.521.

[75] D. D. Miller and E. W. Brown, “Artificial Intelligence in Medical Practice: The Question to the Answer?,” *Am. J. Med.*, vol. 131, no. 2, pp. 129–133, Feb. 2018, doi: 10.1016/j.amjmed.2017.10.035.

[76] J. A. Nichols, H. W. Herbert Chan, and M. A. B. Baker, “Machine learning: applications of artificial intelligence to imaging and diagnosis,” *Biophys. Rev.*, vol. 11, no. 1, pp. 111–118, Sep. 2018, doi: 10.1007/s12551-018-0449-9.

[77] Y. LeCun, Y. Bengio, and G. Hinton, “Deep learning,” *Nature*, vol. 521, no. 7553, pp. 436–444, May 2015, doi: 10.1038/nature14539.

[78] R. B. van Heeswijk, G. Bonanno, S. Coppo, A. Coristine, T. Kober, and M. Stuber, “Motion compensation strategies in magnetic resonance imaging,” *Crit. Rev. Biomed. Eng.*, vol. 40, no. 2, pp. 99–119, 2012, doi: 10.1615/critrevbiomedeng.v40.i2.20.

[79] G. Muscogiuri *et al.*, “Feasibility of late gadolinium enhancement (LGE) in ischemic cardiomyopathy using 2D-multisegment LGE combined with artificial intelligence reconstruction deep learning noise reduction algorithm,” *Int. J. Cardiol.*, vol. 343, pp. 164–170, Nov. 2021, doi: 10.1016/j.ijcard.2021.09.012.

[80] J. Schlemper, J. Caballero, J. V. Hajnal, A. N. Price, and D. Rueckert, “A Deep Cascade of Convolutional Neural Networks for Dynamic MR Image Reconstruction,” *IEEE Trans. Med. Imaging*, vol. 37, no. 2, pp. 491–503, Feb. 2018, doi: 10.1109/TMI.2017.2760978.

[81] R. M. Lebel, “Performance characterization of a novel deep learning-based MR image reconstruction pipeline,” Aug. 14, 2020, *arXiv*: arXiv:2008.06559. doi: 10.48550/arXiv.2008.06559.

[82] M. Frick *et al.*, “Fully automatic geometry planning for cardiac MR imaging and reproducibility of functional cardiac parameters,” *J. Magn. Reson. Imaging JMRI*, vol. 34, no. 2, pp. 457–467, Aug. 2011, doi: 10.1002/jmri.22626.

[83] S. Nitta *et al.*, “Automatic slice alignment method for cardiac magnetic resonance imaging,” *Magma N. Y. N*, vol. 26, no. 5, pp. 451–461, Oct. 2013, doi: 10.1007/s10334-012-0361-4.

[84] “Automatic slice-alignment method in cardiac magnetic resonance imaging for evaluation of the right ventricle in patients with pulmonary hypertension | AIP Advances | AIP Publishing.” Accessed: Mar. 13, 2024. [Online]. Available: https://pubs.aip.org/aip/adv/article/5/9/097182/901806/Automatic-slice-alignment-method-in-cardiac

[85] X. Lu *et al.*, “Automatic view planning for cardiac MRI acquisition,” *Med. Image Comput. Comput.-Assist. Interv. MICCAI Int. Conf. Med. Image Comput. Comput.-Assist. Interv.*, vol. 14, no. Pt 3, pp. 479–486, 2011, doi: 10.1007/978-3-642-23626-6_59.

[86] W. E. Moody *et al.*, “Variation in cardiovascular magnetic resonance myocardial contouring: Insights from an international survey,” *J. Magn. Reson. Imaging*, vol. 50, no. 4, pp. 1336–1338, Oct. 2019, doi: 10.1002/jmri.26689.

[87] P. Peng, K. Lekadir, A. Gooya, L. Shao, S. E. Petersen, and A. F. Frangi, “A review of heart chamber segmentation for structural and functional analysis using cardiac magnetic resonance imaging,” *Magma N. Y. N*, vol. 29, no. 2, pp. 155–195, Apr. 2016, doi: 10.1007/s10334-015-0521-4.

[88] C. Petitjean and J.-N. Dacher, “A review of segmentation methods in short axis cardiac MR images,” *Med. Image Anal.*, vol. 15, no. 2, pp. 169–184, Apr. 2011, doi: 10.1016/j.media.2010.12.004.

[89] O. Ronneberger, P. Fischer, and T. Brox, “U-Net: Convolutional Networks for Biomedical Image Segmentation”.

[90] “Myocardial segmentation in cardiac magnetic resonance images using fully convolutional neural networks | Semantic Scholar.” Accessed: Mar. 14, 2024. [Online]. Available: https://www.semanticscholar.org/paper/Myocardial-segmentation-in-cardiac-magnetic-images-Romaguera-Romero/0c9d755f13d6cd054feb1cff45710145080ff640

[91] W. Bai *et al.*, “Automated cardiovascular magnetic resonance image analysis with fully convolutional networks,” *J. Cardiovasc. Magn. Reson. Off. J. Soc. Cardiovasc. Magn. Reson.*, vol. 20, no. 1, p. 65, Sep. 2018, doi: 10.1186/s12968-018-0471-x.

[92] X. Du *et al.*, “Deep Regression Segmentation for Cardiac Bi-Ventricle MR Images,” vol. 6, 2018.

[93] L. K. Tan, R. A. McLaughlin, E. Lim, Y. F. Abdul Aziz, and Y. M. Liew, “Fully automated segmentation of the left ventricle in cine cardiac MRI using neural network regression,” *J. Magn. Reson. Imaging JMRI*, vol. 48, no. 1, pp. 140–152, Jul. 2018, doi: 10.1002/jmri.25932.

[94] H. El Aidi *et al.*, “Cardiac magnetic resonance imaging findings and the risk of cardiovascular events in patients with recent myocardial infarction or suspected or known coronary artery disease: a systematic review of prognostic studies,” *J. Am. Coll. Cardiol.*, vol. 63, no. 11, pp. 1031–1045, Mar. 2014, doi: 10.1016/j.jacc.2013.11.048.

[95] B. Ambale-Venkatesh *et al.*, “Cardiovascular Event Prediction by Machine Learning: The Multi-Ethnic Study of Atherosclerosis,” *Circ. Res.*, vol. 121, no. 9, pp. 1092–1101, Oct. 2017, doi: 10.1161/CIRCRESAHA.117.311312.

[96] I. H. Sarker, “Machine Learning: Algorithms, Real-World Applications and Research Directions,” *SN Comput. Sci.*, vol. 2, no. 3, p. 160, Mar. 2021, doi: 10.1007/s42979-021-00592-x.

[97] “Foundations of Machine Learning,” MIT Press. Accessed: Mar. 29, 2024. [Online]. Available: https://mitpress.mit.edu/9780262039406/foundations-of-machine-learning/

[98] S. S. Yadav and S. M. Jadhav, “Deep convolutional neural network based medical image classification for disease diagnosis,” *J. Big Data*, vol. 6, no. 1, p. 113, Dec. 2019, doi: 10.1186/s40537-019-0276-2.

[99] M. W. Wagner, K. Namdar, A. Biswas, S. Monah, F. Khalvati, and B. B. Ertl-Wagner, “Radiomics, machine learning, and artificial intelligence—what the neuroradiologist needs to know,” *Neuroradiology*, vol. 63, no. 12, pp. 1957–1967, 2021, doi: 10.1007/s00234-021-02813-9.

[100] S. Raschka, “Model Evaluation, Model Selection, and Algorithm Selection in Machine Learning,” Nov. 10, 2020, *arXiv*: arXiv:1811.12808. doi: 10.48550/arXiv.1811.12808.

[101] L. Breiman, “Random Forests,” *Mach. Learn.*, vol. 45, no. 1, pp. 5–32, Oct. 2001, doi: 10.1023/A:1010933404324.

[102] J. R. Quinlan, “Induction of decision trees,” *Mach. Learn.*, vol. 1, no. 1, pp. 81–106, Mar. 1986, doi: 10.1007/BF00116251.

[103] I. Guyon and A. Elisseeff, “An Introduction to Variable and Feature Selection,” *J. Mach. Learn. Res.*, vol. 3, no. Mar, pp. 1157–1182, 2003.

[104] W. Zhang, Y. Guo, and Q. Jin, “Radiomics and Its Feature Selection: A Review,” *Symmetry*, vol. 15, no. 10, Art. no. 10, Oct. 2023, doi: 10.3390/sym15101834.

[105]M. B. Kursa and W. R. Rudnicki, “Feature Selection with the Boruta Package,” *J. Stat. Softw.*, vol. 36, pp. 1–13, Sep. 2010, doi: 10.18637/jss.v036.i11.

2 Chapter 2: Original Research Manuscript

2.1 Foreword

OS-CMR has been validated as a non-invasive imaging modality that, in conjunction with vasoactive breathing maneuvers, assess vascular function without the need for gadolinium-based contrast agents or pharmaceutical vasodilators. The quantitative characterization of the myocardium in these images can provide invaluable information. Radiomics extends this capability by characterizing the myocardium in terms of shape, intensity, and texture, offering a multifaceted view of the myocardium. When coupled with machine learning techniques, several studies have demonstrated the ability of radiomics to enhance diagnostic accuracy and predictive capabilities.

The following chapter is an original research manuscript. This chapter includes the methodology used in this research and explains the integration of radiomics and machine learning with OS-CMR imaging. It outlines the procedural steps undertaken, presents the results obtained from this approach, and discusses its potential clinical implications.

2.2 Original Research Manuscript

A Radiomics-based Machine Learning Approach for Identification of Ischemic Cardiomyopathy in Oxygenation-Sensitive Cardiovascular Magnetic Resonance Images

2.2.1 Abstract

Background: Oxygenation-sensitive cardiovascular magnetic resonance (OS-CMR) is a contrast-free method that enables the evaluation of myocardial oxygenation in a non-invasive manner [21]. OS-CMR is a valuable tool that provides critical information for the diagnosis of cardiovascular diseases such as coronary artery disease (CAD). Medical imaging radiomics is an emerging field that uses processing techniques to extract quantitative features that characterize global and local photometric, geometrical, and textural properties of images [56]. These objective features can be combined with machine learning techniques to automate the assessment of disease. This study aimed to evaluate the potential of radiomic features extracted from OS-CMR images to identify patients with ischemic cardiomyopathy (ICMP).

Methods: The dataset comprised a total of 120 cases, with 60 healthy volunteers (mean age 54 ±8.9 y, 32 male) and 60 individuals with ICMP (mean age 64 ±11.4 y, 53 male). The myocardium from a single mid-ventricular short-axis (SAX) slice captured across different phases of the cardiac cycle were used for feature extraction. The Pyradiomics python package was used to compute 1021 radiomic features from each stack. Boruta feature selection was performed to identify 37 highly salient features. These were subsequently used to train a Random Forest classifier to distinguish between healthy and ICMP cases. Finally, a SHapley Additive exPlanations (SHAP) analysis was used to rank the salient features and explain their interactions with the predicted classes.

Results: We evaluated the model's performance using classification metrics. The model had an overall accuracy of 0.88, precision of 0.91 in detecting ICMP, recall of 0.83, and F1-score of 0.87. These radiomic features cannot be manually measured due to their complex nature and cannot be perceived by the human eye. There is a noted disparity in the selected feature distributions between the healthy and ICMP groups. (Appendix A provides the complete description of imaging features used in this work).

Conclusion: This study demonstrated that radiomic feature extraction on OS-CMR cine images, combined with machine learning techniques, can be used to identify ICMP from healthy cases with high sensitivity and specificity. This method has the potential to efficiently and non-invasively stratify heart conditions in a clinical setting.

2.2.2 Introduction

Cardiovascular diseases remain a leading cause of mortality worldwide, necessitating effective diagnostic tools and treatment strategies [106]. Ischemic Cardiomyopathy (ICMP) is one of the most prevalent and clinically significant disorders. Using cardiovascular MRI (CMR), late gadolinium enhancement (LGE) has been used to visualize myocardial infarcts and thereby diagnose ICMP. , but relies on injected contrast which poses limitations for patients with renal impairment [20]. Additionally, there is concern over gadolinium deposition in the brain [19]. Oxygenation-sensitive cardiovascular magnetic resonance imaging (OS-CMR) has emerged as a non-invasive method for evaluating changes in myocardial oxygenation, offering advantages such as avoiding the need for intravenous contrast agents and pharmaceutical vasodilators [4]. By leveraging the blood oxygenation level-dependent (BOLD) effect, OS-CMR enables direct assessment of myocardial oxygenation changes, providing valuable insights into myocardial ischemia [5]. Previous studies have demonstrated the utility of OS-CMR in identifying cardiovascular pathologies. For instance, Wacker et al. [107] conducted a study involving patients with single-vessel CAD, revealing significantly lower T2* values in myocardial segments supplied by stenosed arteries compared to healthy myocardium. Similarly, Friedrich et al. [22] reported a mean signal intensity decrease during adenosine stress in myocardial segments related to severe coronary stenoses, showcasing the diagnostic potential of OS-CMR. Moreover, studies by Bernhardt et al. [108], Manka et al. [109], Karamitsos et al. [110], Arnold et al. [111], Jahnke et al. [112], and Walcher et al. [113] further corroborated the effectiveness of OS-CMR in detecting myocardial perfusion deficits and ischemia in CAD cohorts. These studies collectively highlight the promising role of OS-CMR as a non-invasive imaging modality for diagnosing ICMP and other cardiac pathologies.

Radiomics is a method in medical imaging where a large number of quantitative imaging markers are computed from images, followed by the extraction of significant diagnostic or

prognostic features using various algorithms. Originally introduced in computed tomography (CT), radiomics has significantly expanded into MRI, including CMR. This technique has demonstrated its utility in offering innovative markers for various cardiovascular diseases. For example, features like Gray Level Non-Uniformity and T2 kurtosis have shown diagnostic potential in myocarditis and heart failure [114]. Additionally, other features such as the run-length matrix and local binary pattern have provided incremental diagnostic value in differentiating between hypertensive heart disease and hypertrophic cardiomyopathy [9].

The present study aimed to use the potential of radiomics-based analysis of OS-CMR images to discriminate between healthy individuals and patients with ICMP. ICMP, presents imaging features that may be captured through radiomic analysis. By extracting a comprehensive set of radiomic features and employing machine learning algorithms, we attempted to develop a diagnostic model capable of accurately distinguishing ICMP from healthy controls. Overall, this study contributes to the growing body of research exploring the utility of radiomics in cardiovascular imaging.

2.2.3 Methods

2.2.3.1 Study Population

This retrospective study was conducted using data collected at the Royal Victoria Hospital of the McGill University Health Centre. Among the 60 ICMP cases included in the study, 31 were confirmed to have ICMP based on MRI findings, angiography results, and medical history, while 29 self-reported a history of myocardial infarction. Additionally, 60 healthy cases were included in the study, all of whom had no history of relevant medical conditions.

2.2.3.2 OS-CMR Protocol

CMR scans were conducted using a clinical 3 Tesla MRI scanner (Premier, GE Healthcare, Illinois, USA). Subjects were instructed to fast for 4 hours and avoid caffeine intake for 12 hours. A vasoactive breathing maneuver was performed in the exam. CMR images were obtained in basal and mid-ventricular short-axis slices using a triggered modified SSFP sequence. Cine images were continuously acquired during the exam, including a baseline during free breathing over 120 seconds, 60 seconds of metronome-paced hyperventilation at 30 breaths/min, and up to 60 seconds during a long breath-hold.

2.2.3.3 Image Analysis and Preprocessing

Post-hyperventilation breath-hold images were then extracted. Using one mid-ventricular slice, a single cardiac cycle consisting of 20 frames was extracted for radiomic feature extraction. We did not include the basal slices and analysis was performed exclusively on the mid-ventricular slices. This decision was made to maintain consistency and focus on the region with the highest signal quality and reliability for the radiomic measurements required by our study. Using a prototype version of the certified software cvi42™ (Circle Cardiovascular Imaging, Calgary, Canada), an automated segmentation process was employed to segment the myocardium. Subsequently, the images and masks of the myocardium were converted from DICOM format to NIfTI format to have all the frames in a single stack.

Preprocessing steps were performed using PyRadiomics python library (v3.0.1) [64]. The gray-level intensity values of the images were normalized, and discretization was then conducted using a bin width of 20. Resampling was performed to achieve uniform pixel spacing, with a resolution of [1 mm, 1 mm, 1 mm] applied. A grid search was performed to optimize parameters such as bin width for discretization and resampling resolution.

2.2.3.4 Radiomics Feature Extraction

All available radiomic features were extracted from both original and filtered images of the myocardium. Filtering included Laplacian of Gaussian filtering (for sigma = 3.0 and 5.0) and wavelet decomposition. These features cover a wide range and fall into different categories, such as basic histogram analysis, shape-based features, and texture features including Gray Level Co-occurrence Matrix (GLCM), Gray Level Run Length Matrix (GLRLM), Gray Level Size Zone Matrix (GLSZM), Neighboring Gray Tone Difference Matrix (NGTDM), and Gray Level Dependence Matrix (GLDM). For more details about the nature of these features, refer to Section 1.4 and Appendix A which provides the complete description of imaging features used in this work.

2.2.3.5 Machine Learning Pipeline

The dataset was divided randomly into training and testing sets using an 80/20 split, resulting in 96 cases for training and 24 for testing. This ensured an equal representation of both classes in both groups, with 12 healthy and 12 ICMP cases in each. Radiomic feature selection from the training set was performed using the Boruta algorithm.

Several classification algorithms were then employed, including Support Vector Machines (SVM), XGBoost, Logistic Regression, and Random Forest. Random Forest was selected due to its superior accuracy, precision, and recall. The model was trained on the selected features from the training set and subsequently evaluated on the test set.

Both model training and feature selection were conducted using the Scikit-learn and Boruta Python packages. Additionally, to provide insights into the model's predictions, Shapley values were computed for each feature using the SHAP Python package [115]. The workflow is illustrated in Figure 1.

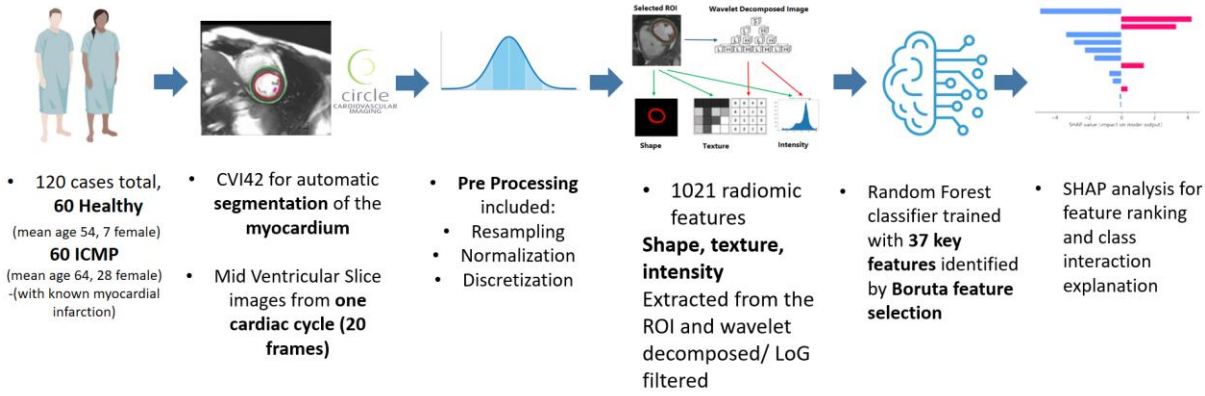

Figure 1 : Overall workflow including the pipeline for feature extraction and model training

2.2.3.5 Statistical Analysis

Continuous data are depicted as the mean ± standard deviation, while categorical data are presented as counts. The chi-square test was used to assess differences in sex distribution between the healthy and ICMP cases, and the Mann-Whitney U test was used to analyze age, BMI, height, and weight discrepancies between the two groups. An unpaired t-test was conducted to compare the selected radiomic feature values between the healthy and ICMP groups, with a significance level set at $p < 0.05$. All statistical tests were performed using Python.

Classifier's performance was assessed using accuracy, precision, recall, and F1-score. Accuracy measures the proportion of correctly classified instances out of the total. Precision assesses the accuracy of positive predictions, indicating the proportion of correctly predicted positive cases among all predicted positives. Recall, on the other hand, evaluates the model's ability to correctly identify positive instances among all actual positives. Lastly, the F1-score, a harmonic mean of precision and recall, offers a balanced assessment of the classifier's performance, considering both false positives and false negatives. Receiver operating characteristic (ROC) curves, precision-recall curves, and calibration curves were generated to further assess the classifier's performance.

2.2.4 Results

2.2.4.1 Baseline Demographic Characteristics

Table 1 provides a comparison of baseline characteristics between ICMP patients and healthy controls. The mean age of healthy controls was 54.4±8.9 years, whereas ICMP patients had a significantly higher mean age of 64.9±11.4 years ($p < 0.001$). The proportion of females was significantly higher among ICMP patients, accounting for 46.6% of the group, compared to only 11.6% in the healthy control group ($p < 0.001$, Chi-square test). Further analysis showed no significant difference in BMI, with healthy controls having an average BMI of 27.87±4.27 kg/m^2 compared to 29.79±5.30 kg/m^2 for ICMP patients (p=0.21). Similarly, differences in weight and height between the groups were not statistically significant, with weights being 82.15±15.26 kg for healthy controls and 85±18.59 kg for ICMP patients (p=0.42, Mann-Whitney test), and heights averaging 1.72±0.10 m for healthy controls versus 1.71±0.09 m for ICMP patients ($p = 0.94$).

Table 1: Baseline characteristics for ICMP patients and healthy controls

Characteristics	Healthy Controls (n=60)	ICMP Patients (n=60)	p-value
Age (years)	54.4±8.9	64.9±11.4	<0.001
Female Sex (n)	7 (11.6%)	28 (46.6%)	<0.001
BMI (kg/m^2)	27.87±4.27	29.79±5.30	0.21
Weight (kg)	82.15±15.26	85±18.59	0.42
Height (m)	1.72±0.10	1.71±0.09	0.94

2.2.4.2 Model Performance Evaluation

A total of 1021 radiomic features were initially extracted from the mid ventricular myocardium segments. Through the Boruta feature selection algorithm, 37 features were identified as salient for further analysis. Meaning and description of these features are provided in Appendix A.

These selected features are summarized in *Table 2*, providing their names, respective classes, and the source image. The table showcases that salient features were predominantly extracted from wavelet-decomposed images, demonstrating the utility of this method in isolating significant characteristics. Additionally, the table also indicates that GLDM features were particularly discriminative, suggesting their effectiveness in capturing key differences in tissue textures between healthy and ICMP cases. *Table 3* presents the means and standard deviations of the feature values in the two groups, along with the corresponding p-values obtained from an unpaired t-test. Thirty-six of these 37 features demonstrated statistical significance (p-value<0.05).

Following the feature selection results, *Figure 2* provides a visual representation of the impact each feature has on the model's output, using SHAP (SHapley Additive exPlanations) values. Each dot on the plot represents a SHAP value for a feature for an individual sample. The horizontal location of a dot shows the impact of that value on the model's prediction, with features pushing the prediction higher shown to the right and those pushing it lower to the left. The vertical axis is ordered according to the features' average impact on the model output, with the topmost features having the highest importance.

The model showed an accuracy of 0.88, accurately predicting 10 out of 12 ICMP cases and 11 out of 12 healthy cases. The confusion matrix depicting these results is presented in *Table 4*, while *Table 5* provides detailed classification metrics derived from it. The classifier achieved a precision of 0.85 for healthy cases and 0.91 for ICMP cases. This indicates a high rate of true positives from all positive predictions. Recall, or the true positive rate, stands at 0.92 for healthy cases and 0.83 for ICMP, showing the model's strength in capturing the majority of actual positive instances. The F1-Score, which harmonizes precision and recall, is recorded at 0.88 for healthy cases and 0.87 for ICMP, showing the balanced accuracy of the model across both classes.

Figure 3 illustrates the ROC curve, having an AUC of 0.92, indicating a high degree of discriminative ability. The precision-recall curve, showing the trade-off between precision and recall, is depicted in *Figure 4*. The high precision across all levels of recall in this curve indicates that the model reliably identifies positive cases (ICMP cases) and maintains high confidence in its predictions.

The calibration curve of the trained classifier is shown in *Figure 5*, compared to that of a perfectly calibrated model. Points below the dashed line show where the classifier is underconfident and predicts lower probabilities than the true outcomes. Points above indicate overconfidence, with the classifier assigning higher probabilities than the actual outcomes. The curve suggests that the classifier is well-calibrated for lower probabilities up to 0.2, then becomes slightly overconfident in the probability ranges around 0.4 and 0.6, and returns to being well-calibrated as the probabilities near 1.0.

Table 2 : List of selected features by feature class and source image, including original, wavelet transformed, and Laplacian of Gaussian-filtered (LoG) images.

Feature Name	Feature Class	Source Image
Flatness	Shape	Original
Maximum 3D Diameter	Shape	Original
Mesh Volume	Shape	Original
Voxel Volume	Shape	Original
Gray Level Non-Uniformity	GLRLM	Original
Coarseness	NGTDM	Original
Dependence Non-Uniformity	GLDM	Wavelet (low-low-high pass filter)
Gray Level Non-Uniformity	GLDM	Wavelet (low-low-high pass filter)
Gray Level Non-Uniformity	GLRLM	Wavelet (low-low-high pass filter)
Coarseness	NGTDM	Wavelet (low-low-high pass filter)
Gray Level Non-Uniformity	GLDM	Wavelet (low-high-low pass filter)
Run Entropy	GLRLM	Wavelet (low-high-low pass filter)
Run Length Non-Uniformity	GLRLM	Wavelet (low-high-low pass filter)
Dependence Non-Uniformity	GLDM	Wavelet (low-high-high pass filter)
Gray Level Non-Uniformity	GLDM	Wavelet (low-high-high pass filter)
Gray Level Non-Uniformity	GLRLM	Wavelet (low-high-high pass filter)
Run Length Non-Uniformity	GLRLM	Wavelet (low-high-high pass filter)
Coarseness	NGTDM	Wavelet (low-high-high pass filter)
Gray Level Non-Uniformity	GLDM	Wavelet (high-low-low pass filter)
Run Length Non-Uniformity	GLRLM	Wavelet (high-low-low pass filter)
Dependence Non-Uniformity	GLDM	Wavelet (high-low-high pass filter)
Gray Level Non-Uniformity	GLDM	Wavelet (high-low-high pass filter)
Gray Level Non-Uniformity	GLRLM	Wavelet (high-low-high pass filter)
Run Length Non-Uniformity	GLRLM	Wavelet (high-low-high pass filter)
Coarseness	NGTDM	Wavelet (high-low-high pass filter)
Dependence Non-Uniformity	GLDM	Wavelet (high-high-low pass filter)
Gray Level Non-Uniformity	GLDM	Wavelet (high-high-low pass filter)
Run Length Non-Uniformity	GLRLM	Wavelet (high-high-low pass filter)
Maximum	First Order	Wavelet (high-high-high pass filter)
Dependence Non-Uniformity	GLDM	Wavelet (high-high-high pass filter)
Gray Level Non-Uniformity	GLDM	Wavelet (high-high-high pass filter)
Gray Level Non-Uniformity	GLRLM	Wavelet (high-high-high pass filter)
Run Length Non-Uniformity	GLRLM	Wavelet (high-high-high pass filter)
Coarseness	NGTDM	Wavelet (high-high-high pass filter)
Complexity	NGTDM	Wavelet (high-high-high pass filter)
Contrast	NGTDM	Wavelet (high-high-high pass filter)
Dependence Non-Uniformity	GLDM	LoG (sigma = 5)

Table 3 : Calculated means and standard deviations of the selected features for both groups and p-values for comparison between groups

Feature Names	**Healthy (n = 60)**	**ICMP (n = 60)**	**p-value**
original_shape_Flatness	0.53 ± 0.05	0.44 ± 0.06	< 0.001
original_shape_Maximum3DDiameter	43.10 ± 3.64	50.02 ± 5.16	< 0.001
original_shape_MeshVolume	9303.26 ± 1877.78	13147.79 ± 2731.14	< 0.001
original_shape_VoxelVolume	9347.06 ± 1879.79	13202.67 ± 2738.07	< 0.001
original_glrlm_GrayLevelNonUniformity	1411.89 ± 243.92	1827.09 ± 379.92	< 0.001
original_ngtdm_Coarseness	0.0013 ± 0.0003	0.0010 ± 0.0004	< 0.001
wavelet-LLH_gldm_DependenceNonUniformity	488.11 ± 97.79	721.29 ± 182.33	< 0.001
wavelet-LLH_gldm_GrayLevelNonUniformity	3722.78 ± 826.38	5677.65 ± 1551.06	< 0.001
wavelet-LLH_glrlm_GrayLevelNonUniformity	1845.58 ± 391.63	2830.31 ± 789.49	< 0.001
wavelet-LLH_ngtdm_Coarseness	0.0007 ± 0.0002	0.0005 ± 0.0002	< 0.001
wavelet-LHL_gldm_GrayLevelNonUniformity	4282.80 ± 1063.80	6076.41 ± 1590.73	< 0.001
wavelet-LHL_glrlm_RunEntropy	3.23 ± 0.14	3.31 ± 0.16	0.0064
wavelet-LHL_glrlm_RunLengthNonUniformity	1953.59 ± 343.13	2581.45 ± 489.98	< 0.001
wavelet-LHH_gldm_DependenceNonUniformity	709.94 ± 157.51	1051.80 ± 255.01	< 0.001
wavelet-LHH_gldm_GrayLevelNonUniformity	4618.30 ± 954.37	6509.76 ± 1397.02	< 0.001
wavelet-LHH_glrlm_GrayLevelNonUniformity	2673.42 ± 529.83	3716.33 ± 769.40	< 0.001
wavelet-LHH_glrlm_RunLengthNonUniformity	2330.41 ± 420.60	3189.21 ± 596.14	< 0.001
wavelet-LHH_ngtdm_Coarseness	0.0005 ± 0.0001	0.0003 ± 0.0001	< 0.001
wavelet-HLL_gldm_GrayLevelNonUniformity	4299.18 ± 1022.16	6164.94 ± 1603.23	< 0.001
wavelet-HLL_glrlm_RunLengthNonUniformity	1926.74 ± 344.12	2475.47 ± 427.49	< 0.001
wavelet-HLH_gldm_DependenceNonUniformity	724.33 ± 148.78	1067.98 ± 252.31	< 0.001
wavelet-HLH_gldm_GrayLevelNonUniformity	4619.26 ± 937.79	6536.05 ± 1386.57	< 0.001
wavelet-HLH_glrlm_GrayLevelNonUniformity	2684.04 ± 512.58	3742.42 ± 762.69	< 0.001
wavelet-HLH_glrlm_RunLengthNonUniformity	2346.72 ± 418.01	3191.89 ± 601.02	< 0.001
wavelet-HLH_ngtdm_Coarseness	0.0005 ± 0.0001	0.0003 ± 0.0001	< 0.001
wavelet-HHL_gldm_DependenceNonUniformity	629.50 ± 139.00	942.39 ± 228.31	< 0.001
wavelet-HHL_gldm_GrayLevelNonUniformity	4650.48 ± 958.58	6556.22 ± 1415.56	< 0.001
wavelet-HHL_glrlm_RunLengthNonUniformity	2025.68 ± 357.34	2768.89 ± 503.13	< 0.001
wavelet-HHH_firstorder_Maximum	16.37 ± 6.61	18.93 ± 9.16	0.0829
wavelet-HHH_gldm_DependenceNonUniformity	825.67 ± 172.59	1211.02 ± 280.23	< 0.001
wavelet-HHH_gldm_GrayLevelNonUniformity	4672.39 ± 941.23	6596.43 ± 1372.18	< 0.001
wavelet-HHH_glrlm_GrayLevelNonUniformity	2805.16 ± 533.17	3882.64 ± 763.08	< 0.001
wavelet-HHH_glrlm_RunLengthNonUniformity	2448.93 ± 437.45	3312.27 ± 611.41	< 0.001
wavelet-HHH_ngtdm_Coarseness	0.0005 ± 0.0001	0.0003 ± 0.0001	< 0.001
wavelet-HHH_ngtdm_Complexity	0.98 ± 0.96	1.81 ± 1.80	0.0020
wavelet-HHH_ngtdm_Contrast	0.10 ± 0.03	0.07 ± 0.04	0.0076
log-sigma-5-0-mm-3D_gldm_DependenceNonUniformity	550.27 ± 158.31	1083.92 ± 534.19	< 0.001

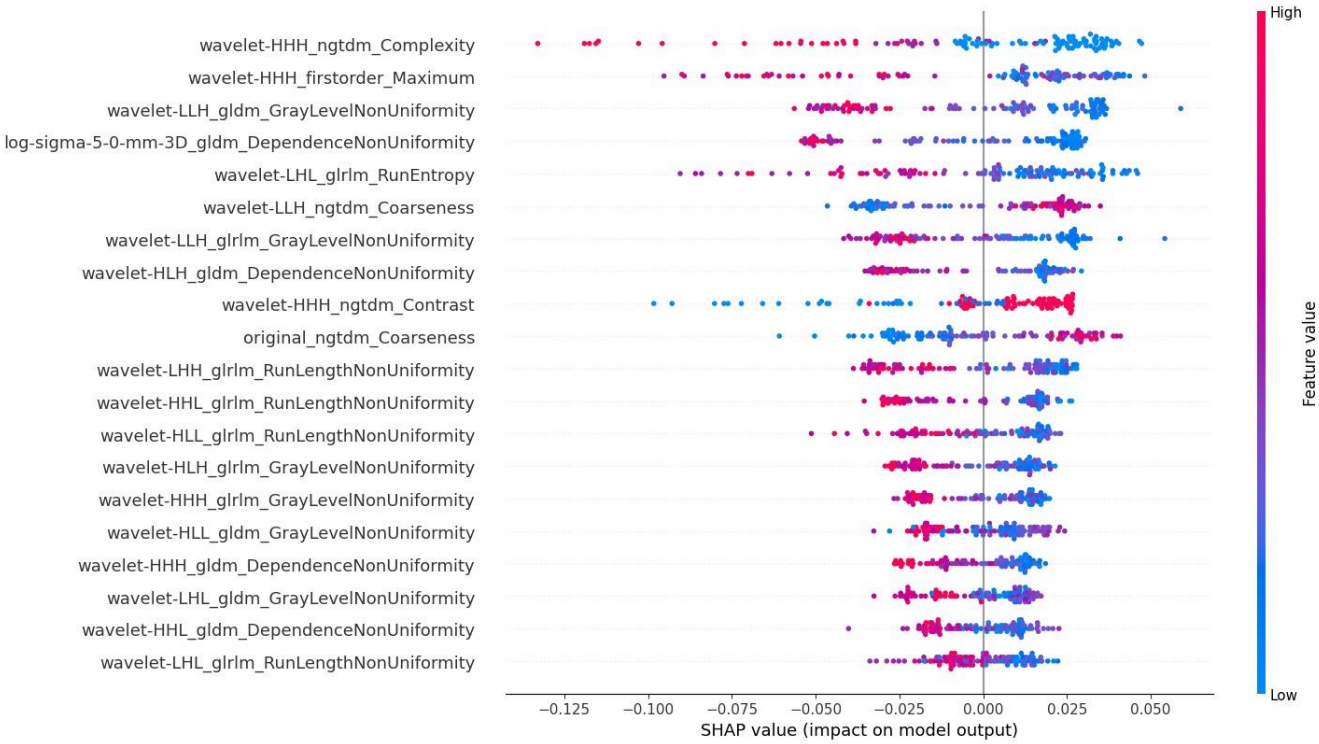

Figure 2 : Beeswarm plot of feature Shapley values in the final model

Table 4 : Confusion matrix for the test set

		Predicted Class	
		Healthy	ICMP
True Class	Healthy	11	1
	ICMP	2	10

Table 5 : Classifier metrics, evaluated on the test set

Class	**Precision**	**Recall**	**F1-Score**
Healthy	0.85	0.92	0.88
ICMP	0.91	0.83	0.87
Weighted Average	0.88	0.88	0.87
		Accuracy:	0.88

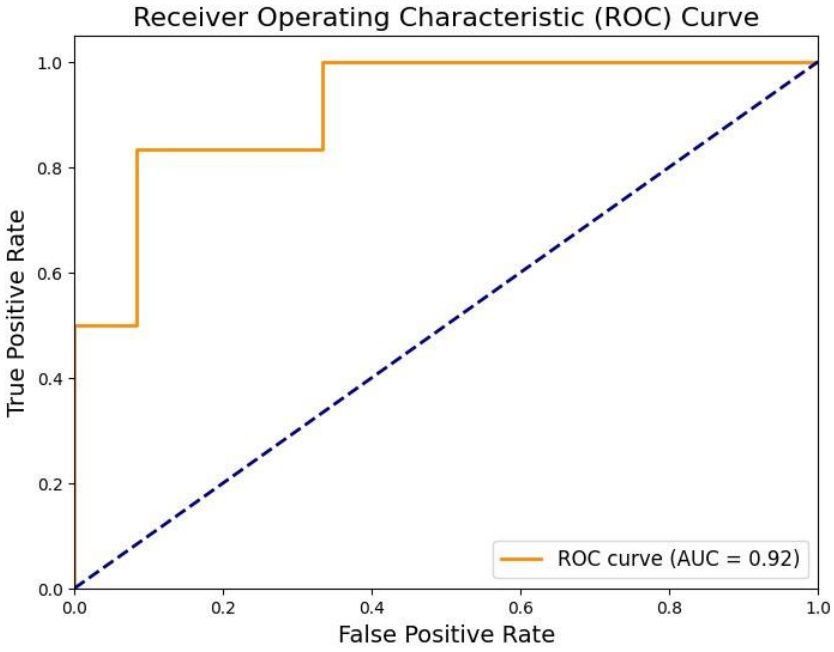

Figure 3 : ROC curve showing the classifier performance in the test set

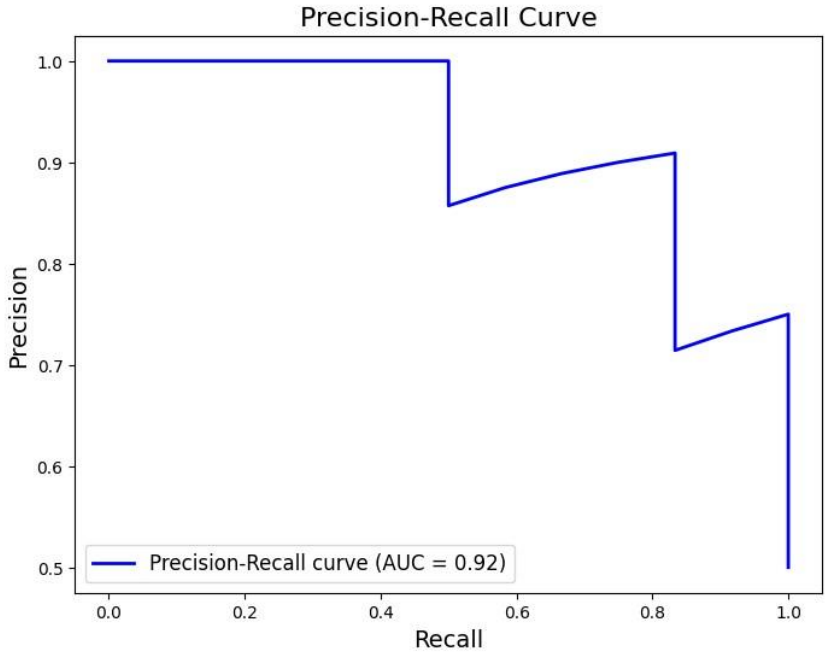

Figure 4 : Precision-Recall curve in the test set

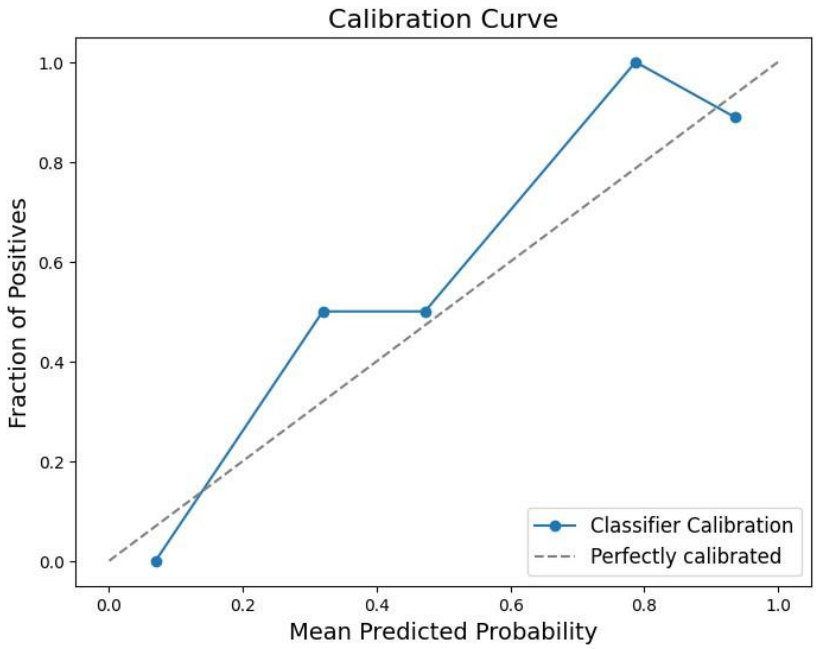

Figure 5 : Calibration curve in the test set

2.2.5 Discussion

This study shows the feasibility of radiomics to automatically distinguish between patients with and without ICMP using OS-CMR images. Our main finding was that our radiomics-based machine learning model was overall 88% accurate in categorizing ICMP and healthy cases based on features extracted from OS-CMR images and had a diagnostic accuracy (AUC) of 92%. Another observation was that wavelet-decomposed images exhibited texture features that were very effective in distinguishing between healthy and ICMP cases.

The main differentiating factor of this study compared to other radiomics studies in CMR imaging lies in the utilization of OS-CMR. Unique to this approach, the analysis was conducted using just one slice and one cardiac cycle, enhancing the impact and specificity of the results. OS-CMR, a 4-minute, non-invasive scan that employs breathing maneuvers without exogenous contrast administration, facilitates the visualization of changes in myocardial oxygenation and enables the detection of ischemia. This innovative approach holds significant promise due to its avoidance of exogenous contrast agents. Unlike current CMR protocols for ICMP, which

typically involve multiple sequences including T1 and T2 maps, LGE, and quantitative perfusion and require at least 40 minutes for completion, OS-CMR offers a more efficient alternative. The ability of our study to detect or rule out ICMP using only a 4-minute scan and a single slice of short-axis cine image is particularly advantageous. By offering a rapid and accessible diagnostic tool, this approach has the potential to change the clinical management of ICMP and optimize healthcare resource utilization.

The retrospective nature of our study introduced limitations that must be considered when interpreting the findings. The machine learning model was trained and tested exclusively on images obtained from a single scanner (Premier™ 3 Tesla, GE Healthcare, Milwaukee, USA), although the test set was isolated. This lack of an external test cohort may potentially compromise the generalizability of our results. Additionally, the dataset used in our analysis exhibited inherent biases, notably in age and sex distributions between healthy individuals and those with ICMP, which could impact the robustness of our conclusions. Furthermore, our comparisons focused on healthy subjects due to the limited representation of other cardiac conditions within our dataset. Future studies would benefit from a more diverse and inclusive cohort to facilitate the distinction between ICMP and other cardiovascular pathologies, thereby enhancing the clinical relevance of our findings. Moreover, it's worth noting that some cases of ICMP relied on self-reported information rather than clinical confirmation, introducing a potential source of uncertainty in our analysis. It is important to note that from the self-reported cases, patients with predominantly right ventricular (RV) ischemia were not excluded from our study, even though only the left ventricle (LV) was segmented. However, isolated RV myocardial infarction (RVMI) is uncommon; more often, RVMI occurs in conjunction with left ventricular MI, particularly when there is inferior wall involvement [116]. Addressing these limitations through prospective studies with larger and more diverse cohorts, as well as

incorporating clinical confirmation for all cases, would strengthen the validity and reliability of our findings.

2.2.6 Conclusions

This study shows that radiomics and machine learning can reliably identify patients with ICMP in OS-CMR images with high diagnostic accuracy and without using contrast agents. This approach could help improve the safety, efficiency and cost-efficiency of the diagnostic workup of patient with suspected heart failure.

2.2.7 References

[21] E. Hillier, J. Covone, and M. G. Friedrich, “Oxygenation-sensitive Cardiac MRI with Vasoactive Breathing Maneuvers for the Non-invasive Assessment of Coronary Microvascular Dysfunction,” *J Vis Exp*, no. 186, Aug. 2022, doi: 10.3791/64149.

[56] “Radiomics: Images Are More than Pictures, They Are Data | Radiology.” Accessed: Feb. 13, 2024. [Online]. Available: https://pubs.rsna.org/doi/full/10.1148/radiol.2015151169

[106] E. J. Benjamin *et al.*, “Heart Disease and Stroke Statistics-2019 Update: A Report From the American Heart Association,” *Circulation*, vol. 139, no. 10, pp. e56–e528, Mar. 2019, doi: 10.1161/CIR.0000000000000659.

[20] F. Martino, G. Amici, M. Rosner, C. Ronco, and G. Novara, “Gadolinium-Based Contrast Media Nephrotoxicity in Kidney Impairment: The Physio-Pathological Conditions for the Perfect Murder,” *J Clin Med*, vol. 10, no. 2, p. 271, Jan. 2021, doi: 10.3390/jcm10020271.

[19] B. J. Guo, Z. L. Yang, and L. J. Zhang, “Gadolinium Deposition in Brain: Current Scientific Evidence and Future Perspectives,” *Front Mol Neurosci*, vol. 11, p. 335, Sep. 2018, doi: 10.3389/fnmol.2018.00335.

[4] C. M. Wacker *et al.*, “Changes in myocardial oxygenation and perfusion under pharmacological stress with dipyridamole: assessment using T*2 and T1 measurements,” *Magn Reson Med*, vol. 41, no. 4, pp. 686–695, Apr. 1999, doi: 10.1002/(sici)1522-2594(199904)41:4<686::aid-mrm6>3.0.co;2-9.

[5] M. G. Friedrich and T. D. Karamitsos, “Oxygenation-sensitive cardiovascular magnetic resonance,” *J Cardiovasc Magn Reson*, vol. 15, no. 1, p. 43, May 2013, doi: 10.1186/1532-429X-15-43.

[107] C. M. Wacker, A. W. Hartlep, S. Pfleger, L. R. Schad, G. Ertl, and W. R. Bauer, “Susceptibility-sensitive magnetic resonance imaging detects human myocardium supplied by a stenotic coronary artery without a contrast agent,” *J Am Coll Cardiol*, vol. 41, no. 5, pp. 834–840, Mar. 2003, doi: 10.1016/s0735-1097(02)02931-5.

[22] M. G. Friedrich, T. Niendorf, J. Schulz-Menger, C. M. Gross, and R. Dietz, “Blood oxygen level-dependent magnetic resonance imaging in patients with stress-induced

angina," *Circulation*, vol. 108, no. 18, pp. 2219–2223, Nov. 2003, doi: 10.1161/01.CIR.0000095271.08248.EA.

[108] P. Bernhardt *et al.*, "Blood oxygen level-dependent magnetic resonance imaging using T2-prepared steady-state free-precession imaging in comparison to contrast-enhanced myocardial perfusion imaging," *Int J Cardiol*, vol. 147, no. 3, pp. 416–419, Mar. 2011, doi: 10.1016/j.ijcard.2009.09.547.

[109] R. Manka, I. Paetsch, B. Schnackenburg, R. Gebker, E. Fleck, and C. Jahnke, "BOLD cardiovascular magnetic resonance at 3.0 tesla in myocardial ischemia," *J Cardiovasc Magn Reson*, vol. 12, no. 1, p. 54, Sep. 2010, doi: 10.1186/1532-429X-12-54.

[110] T. D. Karamitsos *et al.*, "Relationship between regional myocardial oxygenation and perfusion in patients with coronary artery disease: insights from cardiovascular magnetic resonance and positron emission tomography," *Circ Cardiovasc Imaging*, vol. 3, no. 1, pp. 32–40, Jan. 2010, doi: 10.1161/CIRCIMAGING.109.860148.

[111] J. R. Arnold *et al.*, "Myocardial oxygenation in coronary artery disease: insights from blood oxygen level-dependent magnetic resonance imaging at 3 tesla," *J Am Coll Cardiol*, vol. 59, no. 22, pp. 1954–1964, May 2012, doi: 10.1016/j.jacc.2012.01.055.

[112] C. Jahnke, R. Gebker, R. Manka, B. Schnackenburg, E. Fleck, and I. Paetsch, "Navigator-gated 3D blood oxygen level-dependent CMR at 3.0-T for detection of stress-induced myocardial ischemic reactions," *JACC Cardiovasc Imaging*, vol. 3, no. 4, pp. 375–384, Apr. 2010, doi: 10.1016/j.jcmg.2009.12.008.

[113] T. Walcher, R. Manzke, V. Hombach, W. Rottbauer, J. Wöhrle, and P. Bernhardt, "Myocardial perfusion reserve assessed by T2-prepared steady-state free precession blood oxygen level-dependent magnetic resonance imaging in comparison to fractional flow reserve," *Circ Cardiovasc Imaging*, vol. 5, no. 5, pp. 580–586, Sep. 2012, doi: 10.1161/CIRCIMAGING.111.971507.

[114] B. Baessler *et al.*, "Cardiac MRI and Texture Analysis of Myocardial T1 and T2 Maps in Myocarditis with Acute versus Chronic Symptoms of Heart Failure," *Radiology*, vol. 292, no. 3, pp. 608–617, Sep. 2019, doi: 10.1148/radiol.2019190101.

[9] U. Neisius, H. El-Rewaidy, S. Nakamori, J. Rodriguez, W. J. Manning, and R. Nezafat, "Radiomic Analysis of Myocardial Native T1 Imaging Discriminates Between Hypertensive Heart Disease and Hypertrophic Cardiomyopathy," *JACC Cardiovasc Imaging*, vol. 12, no. 10, pp. 1946–1954, Oct. 2019, doi: 10.1016/j.jcmg.2018.11.024.

[64] "Computational Radiomics System to Decode the Radiographic Phenotype - PubMed." Accessed: Mar. 23, 2024. [Online]. Available: https://pubmed.ncbi.nlm.nih.gov/29092951/

[115] S. Lundberg and S.-I. Lee, "A Unified Approach to Interpreting Model Predictions," Nov. 24, 2017, *arXiv*: arXiv:1705.07874. doi: 10.48550/arXiv.1705.07874.

[116] G. Femia, J. K. French, C. Juergens, D. Leung, and S. Lo, "Right ventricular myocardial infarction: pathophysiology, clinical implications and management," *RCM*, vol. 22, no. 4, Art. no. 4, Dec. 2021, doi: 10.31083/j.rcm2204131.

3 Chapter 3: Discussion and Conclusions

3.1 Summary

This concluding chapter discusses the findings of the original research manuscript which explores the potential of OS-CMR, coupled with radiomics techniques, to provide a rapid, non-invasive method for assessing myocardial tissue oxygenation and detecting underlying cardiomyopathies. In addition to summarizing and discussing the findings, this chapter addresses the study's limitations, outlines future directions, and presents conclusions.

The original research manuscript showed significant differences in radiomic features extracted from OS-CMR images between patients with ICMP and healthy controls. The machine learning model trained on these features demonstrates remarkable accuracy, precision, and recall in distinguishing ICMP cases from healthy cases, indicating its potential as a diagnostic tool in clinical practice. The results of this study contribute to the body of evidence supporting the effectiveness of radiomics in cardiovascular imaging. The implications of this for clinical practice are profound, offering an approach for the non-invasive fast detection of ICMP. By using radiomics and machine learning and OS-CMR imaging, clinicians can potentially improve patient care by reducing image acquisition and analysis time, enabling more timely diagnoses.

In conclusion, this thesis highlights the potential of radiomics and machine learning in advancing cardiovascular imaging and disease diagnosis. Further research efforts are necessary to address the limitations of this novel technique and validate the clinical utility of this approach across diverse patient populations.

3.2 Discussion

The findings of this study suggest significant implications for the detection of ICMP. Our results indicate that the application of radiomic analysis on breathing-enhanced OS-CMR images, acquired through a brief, non-contrast 4-minute scan focusing on a single slice, holds promise for the detection of ICMP. This approach offers an efficient means of assessing myocardial tissue characteristics, potentially enabling clinicians to identify subtle pathological changes indicative of ICMP. By leveraging the rich information embedded within a single slice of OS-CMR images, unapparent to human eye, our study shows the potential of radiomics in facilitating diagnosis and intervention for ICMP.

This study was the first to examine radiomics in OS-CMR images, whereas many studies have used radiomics in other types of CMR images to detect different conditions including myocardial ischemia. For instance, in a study by Baesseler et al., it was demonstrated that by using five distinct radiomic texture features, it was possible to distinguish between ischemic scar tissue and normal myocardium on cine CMR images [10]. Avard et al. similarly demonstrated the efficacy of radiomics analysis in accurately detecting myocardial infarction, validating the potential of this approach as an alternative diagnostic method to LGE [67]. In another study, Larroza et al. showed that radiomics texture analysis could differentiate between acute and chronic MI's on both contrast-enhanced and cine CMR images, where MI is frequently difficult to discern visually [117]. These studies exclusively focused on texture features. In contrast, our research included both shape and intensity-based features in addition to texture-based features. While the majority of the identified salient features were texture-based, out of the 37 selected features, three were shape-based.

3.3 Limitations

Radiomics, as a methodology, is reliant on various factors such as the precise segmentation of myocardial tissue, the quality of image acquisition, and the methods used for image reconstruction [118]. In our study, we used the same automatic segmentation algorithm for all images, and all data were acquired from a single scanner. While this approach ensured consistency within our dataset, it may limit the generalizability of our findings to other segmentation techniques and imaging systems. The reliance on a single segmentation algorithm and scanner configuration may introduce biases specific to our dataset, potentially impacting the broader applicability of our results.

Moreover, in this study we did not match healthy controls and ICMP cases on a per-patient basis. Consequently, there is a disparity in the proportion of male participants and the younger age of healthy controls compared to the ICMP cases. This discrepancy may have influenced the radiomic features and prediction outcomes. However, it is crucial to note that despite these differences, the healthy controls did not have any medical conditions known to impact cardiac health. Therefore, while the demographic variations between healthy controls and ICMP cases may have introduced some level of bias into our analysis, the absence of underlying medical conditions that could affect cardiac health ensures the reliability of our study's primary focus on myocardial pathology assessment through radiomic analysis.

Furthermore, in a clinical setting, it would be more beneficial to have a radiomic model that can distinguish between various types of cardiomyopathies, rather than solely identifying ICMP and healthy individuals. However, our study was constrained by the limited availability of patients with OS-CMR scans across different cardiomyopathy subtypes. As a result, our analysis primarily focused on distinguishing ICMP from healthy controls, which represents a simplified scenario compared to the complexity encountered in clinical practice. While this

narrowed scope allowed us to investigate the specific radiomic features associated with ICMP, it is acknowledged that the clinical applicability of our findings may be constrained by the absence of broader cardiomyopathy classifications.

3.4 Future Directions

In future work, expanding the scope of feature selection could enhance the performance and robustness of our model. Incorporating additional features, such as strain parameters related to the dynamic deformation of the heart during the cardiac cycle, could provide valuable insights into myocardial function and could aid in creating more accurate diagnostic models. Moreover, while our study focused solely on radiomic features extracted from the left ventricular myocardium, studies have shown that the inclusion of features related to right ventricular dysfunction and radiomic features related to blood pool signal intensity could also be beneficial in characterizing cardiac pathology [119], [120].

Furthermore, using other advanced techniques such as DL derived features or auto encoder based features could offer additional discriminative power and improve the model's diagnostic capabilities. These approaches have shown remarkable success in various medical imaging applications [121]. Additionally, future research could aim to expand the classification framework to include a broader spectrum of cardiac diseases and pathologies. By refining the model to detect not only ICMP but also other challenging conditions and differentiating between various cardiomyopathies, we can broaden its clinical utility.

The effectiveness of radiomics is significantly influenced by image acquisition parameters, which can substantially alter texture and histogram-based intensity metrics. To ascertain the robustness of these machine learning algorithms for widespread use, future studies should assess datasets from various external cohorts. Additionally, reducing the number of features in

future research might enhance the interpretability of radiomic models, by making it easier to discern the clinical relevance of each feature.

3.5 Conclusions

ICMP is a major global health concern due to its significant mortality. The traditional diagnostic approaches for ICMP are often encumbered by their invasive nature, reliance on contrast agents, or time-intensive protocols. OS-CMR presents an innovative alternative, leveraging the paramagnetic characteristics of deoxygenated hemoglobin within the capillaries to naturally create contrast, thereby avoiding the need for intravenous contrast materials or exposure to ionizing radiation. This technique facilitates the assessment of myocardial oxygenation by tracking the relative shift in oxygen levels in response to induced hyperemia.

OS-CMR can be useful in detecting subtle textural differences in myocardial tissue, which can be quantified through radiomic analysis. The novel research presented in this thesis has explored the viability of employing radiomic features derived from OS-CMR imaging to develop a predictive ML model. The outcomes show that this model is precise and capable of distinguishing between the textural alterations in myocardial tissue associated with healthy hearts and those with ICMP. The promise shown by OS-CMR in capturing these critical changes through radiomic techniques sets a solid foundation for future investigations, which will aim to further enrich the predictive model by incorporating additional data extracted from OS-CMR images.

3.6 References

[10] B. Baessler, M. Mannil, S. Oebel, D. Maintz, H. Alkadhi, and R. Manka, “Subacute and Chronic Left Ventricular Myocardial Scar: Accuracy of Texture Analysis on Nonenhanced Cine MR Images,” *Radiology*, vol. 286, no. 1, pp. 103–112, Jan. 2018, doi: 10.1148/radiol.2017170213.

[67] E. Avard *et al.*, “Non-contrast Cine Cardiac Magnetic Resonance image radiomics features and machine learning algorithms for myocardial infarction detection,” *Computers in Biology and Medicine*, vol. 141, p. 105145, Feb. 2022, doi: 10.1016/j.compbiomed.2021.105145.

[117] A. Larroza, A. Materka, M. P. López-Lereu, J. V. Monmeneu, V. Bodí, and D. Moratal, “Differentiation between acute and chronic myocardial infarction by means of texture analysis of late gadolinium enhancement and cine cardiac magnetic resonance imaging,” *Eur J Radiol*, vol. 92, pp. 78–83, Jul. 2017, doi: 10.1016/j.ejrad.2017.04.024.

[118] J. E. Park, S. Y. Park, H. J. Kim, and H. S. Kim, “Reproducibility and Generalizability in Radiomics Modeling: Possible Strategies in Radiologic and Statistical Perspectives,” *Korean Journal of Radiology*, vol. 20, no. 7, p. 1124, Jul. 2019, doi: 10.3348/kjr.2018.0070.

[119] S. Schalla *et al.*, “Right ventricular function in dilated cardiomyopathy and ischemic heart disease: assessment with non-invasive imaging,” *Neth Heart J*, vol. 23, no. 4, pp. 232–240, Apr. 2015, doi: 10.1007/s12471-015-0673-x.

[120] “Cine MRI-Derived Radiomics Features of the Cardiac Blood Pool: Periodicity, Specificity, and Reproducibility - Lin - 2023 - Journal of Magnetic Resonance Imaging - Wiley Online Library.” Accessed: Apr. 02, 2024. [Online]. Available: https://onlinelibrary.wiley.com/doi/abs/10.1002/jmri.28572

[121] M. Chen, X. Shi, Y. Zhang, D. Wu, and M. Guizani, “Deep Feature Learning for Medical Image Analysis with Convolutional Autoencoder Neural Network,” *IEEE Transactions on Big Data*, vol. PP, pp. 1–1, Jun. 2017, doi: 10.1109/TBDATA.2017.2717439.

Appendix A

This appendix is prepared based on the detailed descriptions and mathematical definitions provided by the PyRadiomics documentation [122].

Shape Features

1. **Flatness**
    - **Formula**:

$$flatness = \sqrt{\frac{\lambda_{least}}{\lambda_{major}}}$$

Where λ_{major} and λ_{least} are the lengths of the largest and smallest principal component axes. Values range from 1 (non-flat, sphere-like) to 0 (flat object, or single-slice segmentation).

Explanation: Measures the flatness of the shape of the ROI.

2. **Maximum 3D Diameter**
    - **Formula**: The largest pairwise Euclidean distance between surface voxels in the ROI.
    - **Explanation**: Indicates the largest distance within the ROI.
3. **Mesh Volume**
    - **Formula**:

$$V_i = \frac{O_{a_i} \cdot (O_{b_i} \times O_{c_i})}{6} \quad (1) \qquad V = \sum_{i=1}^{N_f} V_i \quad (2)$$

The volume of each tetrahedron (V_i) is calculated using the points a_i , b_i , and c_i that define each triangle i of the mesh, along with the image origin (O).

- **Explanation**: The volume of the ROI calculated from the triangle mesh.

4. **Voxel Volume**
   - **Formula**:

$$V_{voxel} = \sum_{k=1}^{N_v} V_k$$

Where V_k is the volume of a single voxel and N is the number of voxels.

- **Explanation**: Total volume occupied by all voxels in the ROI.

Gray Level Run Length Matrix (GLRLM) Features

1. **Gray Level Non-Uniformity (GLN)**
   - **Formula**:

$$GLN = \frac{\sum_{i=1}^{N_g}(\sum_{j=1}^{N_s} P(i,j))^2}{N_z}$$

P(i,j) be the size zone matrix, N_g be the number of discrete intensity values in the image, N_s be the number of discrete zone sizes in the image, N_z be the number of zones in the ROI.

- **Explanation**: Measures the variability of gray-level values in the image with a lower value indicating more homogeneity in intensity values.

2. **Run Entropy**
   - **Formula**:

$$RE = -\sum_{i=1}^{N_g}\sum_{j=1}^{N_r} p(i,j|\theta) log_2(p(i,j|\theta) + \varepsilon)$$

ε is an arbitrarily small positive number. The GLRLM quantifies gray level runs, which are sequences of consecutive pixels with the same gray level value. In a GLRLM P (i , j | θ), the element (i , j) describes the number of runs with gray level i and length j that occur in the image (ROI) along the angle θ. $N_g$is the number of discrete intensity values in the image N_r is the number of discrete run lengths in the image.

Explanation: This reflects the complexity and randomness of the distribution of the lengths of consecutive pixels (runs). A higher entropy value indicates a more complex and less predictable texture pattern.

3. **Run Length Non-Uniformity (RLNU)**
    - **Formula**:

$$RLN = \frac{\sum_{j=1}^{N_r}(\sum_{i=1}^{N_g} P(i,j|\theta))^2}{N_r(\theta)}$$

    - **Explanation**: Measures the similarity of run lengths throughout the image. A lower value shows more homogeneity among run lengths within the image.

Neighborhood Gray Tone Difference Matrix (NGTDM) Features

1. **Coarseness**
    - **Formula**:

$$Coarseness = \frac{1}{\sum_{i=1}^{N_g} p_i s_i}$$

p_i represents the probability of a specific gray level i occurring in the image. s_i is the sum of absolute differences for gray level i , which measures how much the gray level i deviates from a reference value. N_g denotes the number of distinct gray levels present in the image.

- **Explanation**: Coarseness measures the average difference between a center voxel and its surrounding neighborhood, reflecting the rate of spatial change in the texture. A higher coarseness value indicates a slower rate of change, resulting in a more uniform texture in the image.

2. **Complexity**
   - **Formula**:

$$Complexity = \frac{1}{N_{v,p}} \sum_{i=1}^{N_g} \sum_{j=1}^{N_g} |i - j| \frac{p_i s_i + p_j s_j}{p_i + p_j}$$

   - **Explanation**: Quantifies the visual complexity of the texture patterns. An image is considered complex when it has many distinct elements and shows significant variability, with frequent and rapid changes in gray level intensity.

3. **Contrast**
   - **Formula**:

$$Contrast = \left(\frac{1}{N_{g,p}(N_{g,p} - 1)} \sum_{i=1}^{N_g} \sum_{j=1}^{N_g} p_i p_j (i - j)^2\right)\left(\frac{1}{N_{v,p}} \sum_{i=1}^{N_g} s_i\right)$$

$N_{g,p}$ be the number of gray levels that do not have probability of zero. $N_{v,p}$ is the total number of voxels with a valid region.

- **Explanation**: Measures the local variations in the image intensities.

Gray Level Dependence Matrix (GLDM) Features

1. **Dependence Non-Uniformity (DN)**
   - **Formula**:

$$DN = \frac{\sum_{j=1}^{N_d}(\sum_{i=1}^{N_g} P(i,j))^2}{N_z}$$

N_d be the number of discrete dependency sizes in the image. N_z be the number of dependency zones in the image,

   - **Explanation**: Measures the variability of gray-level dependencies in the image, with a lower value indicating more homogeneity among dependencies in the image.

First Order Feature

1. **Maximum**
   - **Formula**:

$$maximum = \max(X)$$

   - **Explanation**: The highest gray-level intensity within the ROI.

Master Reference List

[1] M. A. Khan *et al.*, “Global Epidemiology of Ischemic Heart Disease: Results from the Global Burden of Disease Study,” *Cureus*, vol. 12, no. 7, p. e9349, doi: 10.7759/cureus.9349.

[2] C. Gräni, D. C. Benz, S. Gupta, S. Windecker, and R. Y. Kwong, “Sudden Cardiac Death in Ischemic Heart Disease: From Imaging Arrhythmogenic Substrate to Guiding Therapies,” *JACC Cardiovasc. Imaging*, vol. 13, no. 10, pp. 2223–2238, Oct. 2020, doi: 10.1016/j.jcmg.2019.10.021.

[3] M. Tavakol, S. Ashraf, and S. J. Brener, “Risks and Complications of Coronary Angiography: A Comprehensive Review,” *Glob. J. Health Sci.*, vol. 4, no. 1, pp. 65–93, Jan. 2012, doi: 10.5539/gjhs.v4n1p65.

[4] C. M. Wacker *et al.*, “Changes in myocardial oxygenation and perfusion under pharmacological stress with dipyridamole: assessment using T*2 and T1 measurements,” *Magn. Reson. Med.*, vol. 41, no. 4, pp. 686–695, Apr. 1999, doi: 10.1002/(sici)1522-2594(199904)41:4<686::aid-mrm6>3.0.co;2-9.

[5] M. G. Friedrich and T. D. Karamitsos, “Oxygenation-sensitive cardiovascular magnetic resonance,” *J. Cardiovasc. Magn. Reson.*, vol. 15, no. 1, p. 43, May 2013, doi: 10.1186/1532-429X-15-43.

[6] J. M. Luu, A. Schmidt, J. Flewitt, Y. Mikami, H. Ter Keurs, and M. G. Friedrich, “Cardiovascular risk is associated with a transmural gradient of myocardial oxygenation during adenosine infusion,” *Eur. Heart J. Cardiovasc. Imaging*, vol. 20, no. 11, pp. 1287–1295, Nov. 2019, doi: 10.1093/ehjci/jey202.

[7] B. Baeßler, M. Mannil, D. Maintz, H. Alkadhi, and R. Manka, “Texture analysis and machine learning of non-contrast T1-weighted MR images in patients with hypertrophic cardiomyopathy-Preliminary results,” *Eur. J. Radiol.*, vol. 102, pp. 61–67, May 2018, doi: 10.1016/j.ejrad.2018.03.013.

[8] I. Cetin, S. E. Petersen, S. Napel, O. Camara, M. A. G. Ballester, and K. Lekadir, “A radiomics approach to analyze cardiac alterations in hypertension,” in *2019 IEEE 16th International Symposium on Biomedical Imaging (ISBI 2019)*, Apr. 2019, pp. 640–643. doi: 10.1109/ISBI.2019.8759440.

[9] U. Neisius, H. El-Rewaidy, S. Nakamori, J. Rodriguez, W. J. Manning, and R. Nezafat, “Radiomic Analysis of Myocardial Native T1 Imaging Discriminates Between Hypertensive Heart Disease and Hypertrophic Cardiomyopathy,” *JACC Cardiovasc. Imaging*, vol. 12, no. 10, pp. 1946–1954, Oct. 2019, doi: 10.1016/j.jcmg.2018.11.024.

[10] B. Baessler, M. Mannil, S. Oebel, D. Maintz, H. Alkadhi, and R. Manka, “Subacute and Chronic Left Ventricular Myocardial Scar: Accuracy of Texture Analysis on Nonenhanced Cine MR Images,” *Radiology*, vol. 286, no. 1, pp. 103–112, Jan. 2018, doi: 10.1148/radiol.2017170213.

[11] D. C. Lee *et al.*, “The growth and evolution of cardiovascular magnetic resonance: a 20-year history of the Society for Cardiovascular Magnetic Resonance (SCMR) annual scientific sessions,” *J. Cardiovasc. Magn. Reson.*, vol. 20, p. 8, Jan. 2018, doi: 10.1186/s12968-018-0429-z.

[12] “An Introduction to Magnetic Resonance Imaging: From Image Acquisition to Clinical Diagnosis | Request PDF.” Accessed: Mar. 26, 2024. [Online]. Available:

https://www.researchgate.net/publication/226073222_An_Introduction_to_Magnetic_Resonance_Imaging_From_Image_Acquisition_to_Clinical_Diagnosis

[13] T. A. Gallagher, A. J. Nemeth, and L. Hacein-Bey, “An introduction to the Fourier transform: relationship to MRI,” *AJR Am. J. Roentgenol.*, vol. 190, no. 5, pp. 1396–1405, May 2008, doi: 10.2214/AJR.07.2874.

[14] R. J. Perea *et al.*, “T1 mapping: characterisation of myocardial interstitial space,” *Insights Imaging*, vol. 6, no. 2, pp. 189–202, Nov. 2014, doi: 10.1007/s13244-014-0366-9.

[15] R. Wassmuth *et al.*, “Variability and homogeneity of cardiovascular magnetic resonance myocardial T2-mapping in volunteers compared to patients with edema,” *J. Cardiovasc. Magn. Reson.*, vol. 15, no. 1, p. 27, Mar. 2013, doi: 10.1186/1532-429X-15-27.

[16] F. von Knobelsdorff-Brenkenhoff and J. Schulz-Menger, “Role of cardiovascular magnetic resonance in the guidelines of the European Society of Cardiology,” *J. Cardiovasc. Magn. Reson.*, vol. 18, p. 6, Jan. 2016, doi: 10.1186/s12968-016-0225-6.

[17] “The histologic basis of late gadolinium enhancement cardiovascular magnetic resonance in hypertrophic cardiomyopathy | Journal of the American College of Cardiology.” Accessed: Apr. 13, 2024. [Online]. Available: https://www.jacc.org/doi/abs/10.1016/j.jacc.2004.03.035

[18] H. Satoh *et al.*, “Distribution of late gadolinium enhancement in various types of cardiomyopathies: Significance in differential diagnosis, clinical features and prognosis,” *World J. Cardiol.*, vol. 6, no. 7, pp. 585–601, Jul. 2014, doi: 10.4330/wjc.v6.i7.585.

[19] B. J. Guo, Z. L. Yang, and L. J. Zhang, “Gadolinium Deposition in Brain: Current Scientific Evidence and Future Perspectives,” *Front. Mol. Neurosci.*, vol. 11, p. 335, Sep. 2018, doi: 10.3389/fnmol.2018.00335.

[20] F. Martino, G. Amici, M. Rosner, C. Ronco, and G. Novara, “Gadolinium-Based Contrast Media Nephrotoxicity in Kidney Impairment: The Physio-Pathological Conditions for the Perfect Murder,” *J. Clin. Med.*, vol. 10, no. 2, p. 271, Jan. 2021, doi: 10.3390/jcm10020271.

[21] E. Hillier, J. Covone, and M. G. Friedrich, “Oxygenation-sensitive Cardiac MRI with Vasoactive Breathing Maneuvers for the Non-invasive Assessment of Coronary Microvascular Dysfunction,” *J. Vis. Exp. JoVE*, no. 186, Aug. 2022, doi: 10.3791/64149.

[22] M. G. Friedrich, T. Niendorf, J. Schulz-Menger, C. M. Gross, and R. Dietz, “Blood oxygen level-dependent magnetic resonance imaging in patients with stress-induced angina,” *Circulation*, vol. 108, no. 18, pp. 2219–2223, Nov. 2003, doi: 10.1161/01.CIR.0000095271.08248.EA.

[23] D. P. Guensch *et al.*, “The blood oxygen level dependent (BOLD) effect of in-vitro myoglobin and hemoglobin,” *Sci. Rep.*, vol. 11, p. 11464, Jun. 2021, doi: 10.1038/s41598-021-90908-x.

[24] U. Ikeda, K. Kurosaki, K. Ohya, and K. Shimada, “Adenosine stimulates nitric oxide synthesis in vascular smooth muscle cells,” *Cardiovasc. Res.*, vol. 35, no. 1, pp. 168–174, Jul. 1997, doi: 10.1016/s0008-6363(97)00068-0.

[25] T. Voigtländer *et al.*, “The adverse events and hemodynamic effects of adenosine-based cardiac MRI,” *Korean J. Radiol.*, vol. 12, no. 4, pp. 424–430, 2011, doi: 10.3348/kjr.2011.12.4.424.

[26] J. E. Brian, “Carbon dioxide and the cerebral circulation,” *Anesthesiology*, vol. 88, no. 5, pp. 1365–1386, May 1998, doi: 10.1097/00000542-199805000-00029.

[27] F. C. Moreton, K. A. Dani, C. Goutcher, K. O’Hare, and K. W. Muir, “Respiratory challenge MRI: Practical aspects,” *NeuroImage Clin.*, vol. 11, pp. 667–677, May 2016, doi: 10.1016/j.nicl.2016.05.003.

[28] K. Fischer *et al.*, “Feasibility of cardiovascular magnetic resonance to detect oxygenation deficits in patients with multi-vessel coronary artery disease triggered by breathing maneuvers,” *J. Cardiovasc. Magn. Reson. Off. J. Soc. Cardiovasc. Magn. Reson.*, vol. 20, no. 1, p. 31, May 2018, doi: 10.1186/s12968-018-0446-y.

[29] F. Roubille, K. Fischer, D. P. Guensch, J.-C. Tardif, and M. G. Friedrich, “Impact of hyperventilation and apnea on myocardial oxygenation in patients with obstructive sleep apnea - An oxygenation-sensitive CMR study,” *J. Cardiol.*, vol. 69, no. 2, pp. 489–494, Feb. 2017, doi: 10.1016/j.jjcc.2016.03.011.

[30] M. Elharram *et al.*, “Regional Heterogeneity in the Coronary Vascular Response in Women With Chest Pain and Nonobstructive Coronary Artery Disease,” *Circulation*, vol. 143, no. 7, pp. 764–766, Feb. 2021, doi: 10.1161/CIRCULATIONAHA.120.052520.

[31] D. P. Guensch, K. Fischer, J. A. Flewitt, and M. G. Friedrich, “Impact of intermittent apnea on myocardial tissue oxygenation--a study using oxygenation-sensitive cardiovascular magnetic resonance,” *PloS One*, vol. 8, no. 1, p. e53282, 2013, doi: 10.1371/journal.pone.0053282.

[32] K. Fischer, D. P. Guensch, and M. G. Friedrich, “Response of myocardial oxygenation to breathing manoeuvres and adenosine infusion,” *Eur. Heart J. Cardiovasc. Imaging*, vol. 16, no. 4, pp. 395–401, Apr. 2015, doi: 10.1093/ehjci/jeu202.

[33] E. Hillier, T. Hafyane, and M. Friedrich, “285Myocardial and cerebral oxygenation deficits in heart failure patients - a multi-parametric study,” *Eur. Heart J. - Cardiovasc. Imaging*, vol. 20, Jun. 2019, doi: 10.1093/ehjci/jez114.003.

[34] N. Iannino, K. Fischer, M. Friedrich, T. Hafyane, F.-P. Mongeon, and M. White, “Myocardial Vascular Function Assessed by Dynamic Oxygenation-sensitive Cardiac Magnetic Resonance Imaging Long-term Following Cardiac Transplantation,” *Transplantation*, vol. 105, no. 6, pp. 1347–1355, Jun. 2021, doi: 10.1097/TP.0000000000003419.

[35] K. Fischer, D. P. Guensch, N. Shie, J. Lebel, and M. G. Friedrich, “Breathing Maneuvers as a Vasoactive Stimulus for Detecting Inducible Myocardial Ischemia - An Experimental Cardiovascular Magnetic Resonance Study,” *PloS One*, vol. 11, no. 10, p. e0164524, 2016, doi: 10.1371/journal.pone.0164524.

[36] K. Fischer *et al.*, “Insights Into Myocardial Oxygenation and Cardiovascular Magnetic Resonance Tissue Biomarkers in Heart Failure With Preserved Ejection Fraction,” *Circ. Heart Fail.*, vol. 15, no. 4, p. e008903, Apr. 2022, doi: 10.1161/CIRCHEARTFAILURE.121.008903.

[37] B. Bhandari, B. S. Quintanilla Rodriguez, and W. Masood, “Ischemic Cardiomyopathy,” in *StatPearls*, Treasure Island (FL): StatPearls Publishing, 2024. Accessed: Mar. 08, 2024. [Online]. Available: http://www.ncbi.nlm.nih.gov/books/NBK537301/

[38] P. A. McCullough, “Coronary Artery Disease,” *Clin. J. Am. Soc. Nephrol.*, vol. 2, no. 3, p. 611, May 2007, doi: 10.2215/CJN.03871106.

[39] “Cell Biology of Ischemia/Reperfusion Injury - PMC.” Accessed: Apr. 13, 2024. [Online]. Available: https://www.ncbi.nlm.nih.gov/pmc/articles/PMC3904795/

[40] “Ischemic Cardiomyopathy: What You Need To Know,” Cleveland Clinic. Accessed: Mar. 30, 2024. [Online]. Available: https://my.clevelandclinic.org/health/diseases/17145-ischemic-cardiomyopathy

[41] C. Doesch and T. Papavassiliu, “Diagnosis and management of ischemic cardiomyopathy: Role of cardiovascular magnetic resonance imaging,” *World J. Cardiol.*, vol. 6, no. 11, pp. 1166–1174, Nov. 2014, doi: 10.4330/wjc.v6.i11.1166.

[42] J. Soongswang *et al.*, “Limitation of transthoracic echocardiography in the diagnosis of congenital heart diseases,” *J. Med. Assoc. Thail. Chotmaihet Thangphaet*, vol. 83 Suppl 2, pp. S111-117, Nov. 2000.

[43] M. Egred, G. D. Waiter, T. W. Redpath, S. K. I. Semple, A. Al-Mohammad, and S. Walton, “Blood oxygen level-dependent (BOLD) MRI: A novel technique for the assessment of myocardial ischemia as identified by nuclear imaging SPECT,” *Eur. J. Intern. Med.*, vol. 18, no. 8, pp. 581–586, Dec. 2007, doi: 10.1016/j.ejim.2007.03.013.

[44] P. A. Kaufmann and P. G. Camici, “Myocardial blood flow measurement by PET: technical aspects and clinical applications,” *J. Nucl. Med. Off. Publ. Soc. Nucl. Med.*, vol. 46, no. 1, pp. 75–88, Jan. 2005.

[45] Z. Sun, G. H. Choo, and K. H. Ng, “Coronary CT angiography: current status and continuing challenges,” *Br. J. Radiol.*, vol. 85, no. 1013, pp. 495–510, May 2012, doi: 10.1259/bjr/15296170.

[46] Y. Tanabe *et al.*, “Computed tomographic evaluation of myocardial ischemia,” *Jpn. J. Radiol.*, vol. 38, no. 5, pp. 411–433, 2020, doi: 10.1007/s11604-020-00922-8.

[47] N. S. Nurmohamed *et al.*, “Development and Validation of a Quantitative Coronary CT Angiography Model for Diagnosis of Vessel-Specific Coronary Ischemia,” *JACC Cardiovasc. Imaging*, vol. 17, no. 8, pp. 894–906, Aug. 2024, doi: 10.1016/j.jcmg.2024.01.007.

[48] E. J. Topol and S. E. Nissen, “Our preoccupation with coronary luminology. The dissociation between clinical and angiographic findings in ischemic heart disease,” *Circulation*, vol. 92, no. 8, pp. 2333–2342, Oct. 1995, doi: 10.1161/01.cir.92.8.2333.

[49] A. Scatteia and S. Dellegrottaglie, “Cardiac magnetic resonance in ischemic cardiomyopathy: present role and future directions,” *Eur. Heart J. Suppl.*, vol. 25, no. Supplement_C, pp. C58–C62, May 2023, doi: 10.1093/eurheartjsupp/suad007.

[50] T. Kotecha *et al.*, “Automated Pixel-Wise Quantitative Myocardial Perfusion Mapping by CMR to Detect Obstructive Coronary Artery Disease and Coronary Microvascular Dysfunction: Validation Against Invasive Coronary Physiology,” *JACC Cardiovasc. Imaging*, vol. 12, no. 10, pp. 1958–1969, Oct. 2019, doi: 10.1016/j.jcmg.2018.12.022.

[51] “Assessment of stable coronary artery disease by cardiovascular magnetic resonance imaging: Current and emerging techniques - PMC.” Accessed: Apr. 14, 2024. [Online]. Available: https://www.ncbi.nlm.nih.gov/pmc/articles/PMC5329750/

[52] H. M. Lak, S. Ranka, and A. Goyal, “Pharmacologic Stress Testing,” in *StatPearls*, Treasure Island (FL): StatPearls Publishing, 2024. Accessed: Apr. 14, 2024. [Online]. Available: http://www.ncbi.nlm.nih.gov/books/NBK555963/

[53] Y. M. Shamam and O. De Jesus, “Nephrogenic Systemic Fibrosis,” in *StatPearls*, Treasure Island (FL): StatPearls Publishing, 2024. Accessed: Apr. 14, 2024. [Online]. Available: http://www.ncbi.nlm.nih.gov/books/NBK567754/

[54] M. O. Baerlocher, M. Asch, and A. Myers, “Allergic-type reactions to radiographic contrast media,” *CMAJ Can. Med. Assoc. J.*, vol. 182, no. 12, p. 1328, Sep. 2010, doi: 10.1503/cmaj.090371.

[55] V. Kumar *et al.*, “Radiomics: the process and the challenges,” *Magn. Reson. Imaging*, vol. 30, no. 9, pp. 1234–1248, Nov. 2012, doi: 10.1016/j.mri.2012.06.010.

[56] “Radiomics: Images Are More than Pictures, They Are Data | Radiology.” Accessed: Feb. 13, 2024. [Online]. Available: https://pubs.rsna.org/doi/full/10.1148/radiol.2015151169

[57] A. Wibmer *et al.*, “Haralick texture analysis of prostate MRI: utility for differentiating non-cancerous prostate from prostate cancer and differentiating prostate cancers with different Gleason scores,” *Eur. Radiol.*, vol. 25, no. 10, pp. 2840–2850, Oct. 2015, doi: 10.1007/s00330-015-3701-8.

[58] A. Ahmed, P. Gibbs, M. Pickles, and L. Turnbull, “Texture analysis in assessment and prediction of chemotherapy response in breast cancer,” *J. Magn. Reson. Imaging JMRI*, vol. 38, no. 1, pp. 89–101, Jul. 2013, doi: 10.1002/jmri.23971.

[59] T. P. Coroller *et al.*, “Radiomic-Based Pathological Response Prediction from Primary Tumors and Lymph Nodes in NSCLC,” *J. Thorac. Oncol. Off. Publ. Int. Assoc. Study Lung Cancer*, vol. 12, no. 3, pp. 467–476, Mar. 2017, doi: 10.1016/j.jtho.2016.11.2226.

[60] T. P. Coroller *et al.*, “CT-based radiomic signature predicts distant metastasis in lung adenocarcinoma,” *Radiother. Oncol. J. Eur. Soc. Ther. Radiol. Oncol.*, vol. 114, no. 3, pp. 345–350, Mar. 2015, doi: 10.1016/j.radonc.2015.02.015.

[61] “Decoding tumour phenotype by noninvasive imaging using a quantitative radiomics approach - PubMed.” Accessed: Mar. 30, 2024. [Online]. Available: https://pubmed.ncbi.nlm.nih.gov/24892406/

[62] C. S. Brenner, “B Y D. MARR A N D E. HILDRETH”.

[63] R. S. Pathak, *THE WAVELET TRANSFORM*. Springer Science & Business Media, 2009.

[64] “Computational Radiomics System to Decode the Radiographic Phenotype - PubMed.” Accessed: Mar. 23, 2024. [Online]. Available: https://pubmed.ncbi.nlm.nih.gov/29092951/

[65] P. Lambin *et al.*, “Radiomics: the bridge between medical imaging and personalized medicine,” *Nat. Rev. Clin. Oncol.*, vol. 14, no. 12, pp. 749–762, Dec. 2017, doi: 10.1038/nrclinonc.2017.141.

[66] G. Thibault, J. Angulo, and F. Meyer, “Advanced statistical matrices for texture characterization: application to cell classification,” *IEEE Trans. Biomed. Eng.*, vol. 61, no. 3, pp. 630–637, Mar. 2014, doi: 10.1109/TBME.2013.2284600.

[67] E. Avard *et al.*, “Non-contrast Cine Cardiac Magnetic Resonance image radiomics features and machine learning algorithms for myocardial infarction detection,” *Comput. Biol. Med.*, vol. 141, p. 105145, Feb. 2022, doi: 10.1016/j.compbiomed.2021.105145.

[68] A. S. Fahmy, E. J. Rowin, A. Arafati, T. Al-Otaibi, M. S. Maron, and R. Nezafat, “Radiomics and deep learning for myocardial scar screening in hypertrophic cardiomyopathy,” *J. Cardiovasc. Magn. Reson.*, vol. 24, no. 1, p. 40, Jun. 2022, doi: 10.1186/s12968-022-00869-x.

[69] Y. Amano, Y. Suzuki, F. Yanagisawa, Y. Omori, and N. Matsumoto, “Relationship between Extension or Texture Features of Late Gadolinium Enhancement and

Ventricular Tachyarrhythmias in Hypertrophic Cardiomyopathy," *BioMed Res. Int.*, vol. 2018, p. 4092469, Sep. 2018, doi: 10.1155/2018/4092469.

[70] "Cardiac magnetic resonance image-based classification of the risk of arrhythmias in post-myocardial infarction patients - PubMed." Accessed: Mar. 30, 2024. [Online]. Available: https://pubmed.ncbi.nlm.nih.gov/26239472/

[71] "LGE-CMR-derived texture features reflect poor prognosis in hypertrophic cardiomyopathy patients with systolic dysfunction: preliminary results - PubMed." Accessed: Mar. 30, 2024. [Online]. Available: https://pubmed.ncbi.nlm.nih.gov/29728817/

[72] S. Russell and J. Bohannon, "Artificial intelligence. Fears of an AI pioneer," *Science*, vol. 349, no. 6245, p. 252, Jul. 2015, doi: 10.1126/science.349.6245.252.

[73] C. Krittanawong, H. Zhang, Z. Wang, M. Aydar, and T. Kitai, "Artificial Intelligence in Precision Cardiovascular Medicine," *J. Am. Coll. Cardiol.*, vol. 69, no. 21, pp. 2657–2664, May 2017, doi: 10.1016/j.jacc.2017.03.571.

[74] K. W. Johnson *et al.*, "Artificial Intelligence in Cardiology," *J. Am. Coll. Cardiol.*, vol. 71, no. 23, pp. 2668–2679, Jun. 2018, doi: 10.1016/j.jacc.2018.03.521.

[75] D. D. Miller and E. W. Brown, "Artificial Intelligence in Medical Practice: The Question to the Answer?," *Am. J. Med.*, vol. 131, no. 2, pp. 129–133, Feb. 2018, doi: 10.1016/j.amjmed.2017.10.035.

[76] J. A. Nichols, H. W. Herbert Chan, and M. A. B. Baker, "Machine learning: applications of artificial intelligence to imaging and diagnosis," *Biophys. Rev.*, vol. 11, no. 1, pp. 111–118, Sep. 2018, doi: 10.1007/s12551-018-0449-9.

[77] Y. LeCun, Y. Bengio, and G. Hinton, "Deep learning," *Nature*, vol. 521, no. 7553, pp. 436–444, May 2015, doi: 10.1038/nature14539.

[78] R. B. van Heeswijk, G. Bonanno, S. Coppo, A. Coristine, T. Kober, and M. Stuber, "Motion compensation strategies in magnetic resonance imaging," *Crit. Rev. Biomed. Eng.*, vol. 40, no. 2, pp. 99–119, 2012, doi: 10.1615/critrevbiomedeng.v40.i2.20.

[79] G. Muscogiuri *et al.*, "Feasibility of late gadolinium enhancement (LGE) in ischemic cardiomyopathy using 2D-multisegment LGE combined with artificial intelligence reconstruction deep learning noise reduction algorithm," *Int. J. Cardiol.*, vol. 343, pp. 164–170, Nov. 2021, doi: 10.1016/j.ijcard.2021.09.012.

[80] J. Schlemper, J. Caballero, J. V. Hajnal, A. N. Price, and D. Rueckert, "A Deep Cascade of Convolutional Neural Networks for Dynamic MR Image Reconstruction," *IEEE Trans. Med. Imaging*, vol. 37, no. 2, pp. 491–503, Feb. 2018, doi: 10.1109/TMI.2017.2760978.

[81] R. M. Lebel, "Performance characterization of a novel deep learning-based MR image reconstruction pipeline," Aug. 14, 2020, *arXiv*: arXiv:2008.06559. doi: 10.48550/arXiv.2008.06559.

[82] M. Frick *et al.*, "Fully automatic geometry planning for cardiac MR imaging and reproducibility of functional cardiac parameters," *J. Magn. Reson. Imaging JMRI*, vol. 34, no. 2, pp. 457–467, Aug. 2011, doi: 10.1002/jmri.22626.

[83] S. Nitta *et al.*, "Automatic slice alignment method for cardiac magnetic resonance imaging," *Magma N. Y. N*, vol. 26, no. 5, pp. 451–461, Oct. 2013, doi: 10.1007/s10334-012-0361-4.

[84] “Automatic slice-alignment method in cardiac magnetic resonance imaging for evaluation of the right ventricle in patients with pulmonary hypertension | AIP Advances | AIP Publishing.” Accessed: Mar. 13, 2024. [Online]. Available: https://pubs.aip.org/aip/adv/article/5/9/097182/901806/Automatic-slice-alignment-method-in-cardiac

[85] X. Lu *et al.*, “Automatic view planning for cardiac MRI acquisition,” *Med. Image Comput. Comput.-Assist. Interv. MICCAI Int. Conf. Med. Image Comput. Comput.-Assist. Interv.*, vol. 14, no. Pt 3, pp. 479–486, 2011, doi: 10.1007/978-3-642-23626-6_59.

[86] W. E. Moody *et al.*, “Variation in cardiovascular magnetic resonance myocardial contouring: Insights from an international survey,” *J. Magn. Reson. Imaging*, vol. 50, no. 4, pp. 1336–1338, Oct. 2019, doi: 10.1002/jmri.26689.

[87] P. Peng, K. Lekadir, A. Gooya, L. Shao, S. E. Petersen, and A. F. Frangi, “A review of heart chamber segmentation for structural and functional analysis using cardiac magnetic resonance imaging,” *Magma N. Y. N*, vol. 29, no. 2, pp. 155–195, Apr. 2016, doi: 10.1007/s10334-015-0521-4.

[88] C. Petitjean and J.-N. Dacher, “A review of segmentation methods in short axis cardiac MR images,” *Med. Image Anal.*, vol. 15, no. 2, pp. 169–184, Apr. 2011, doi: 10.1016/j.media.2010.12.004.

[89] O. Ronneberger, P. Fischer, and T. Brox, “U-Net: Convolutional Networks for Biomedical Image Segmentation”.

[90] “Myocardial segmentation in cardiac magnetic resonance images using fully convolutional neural networks | Semantic Scholar.” Accessed: Mar. 14, 2024. [Online]. Available: https://www.semanticscholar.org/paper/Myocardial-segmentation-in-cardiac-magnetic-images-Romaguera-Romero/0c9d755f13d6cd054feb1cff45710145080ff640

[91] W. Bai *et al.*, “Automated cardiovascular magnetic resonance image analysis with fully convolutional networks,” *J. Cardiovasc. Magn. Reson. Off. J. Soc. Cardiovasc. Magn. Reson.*, vol. 20, no. 1, p. 65, Sep. 2018, doi: 10.1186/s12968-018-0471-x.

[92] X. Du *et al.*, “Deep Regression Segmentation for Cardiac Bi-Ventricle MR Images,” vol. 6, 2018.

[93] L. K. Tan, R. A. McLaughlin, E. Lim, Y. F. Abdul Aziz, and Y. M. Liew, “Fully automated segmentation of the left ventricle in cine cardiac MRI using neural network regression,” *J. Magn. Reson. Imaging JMRI*, vol. 48, no. 1, pp. 140–152, Jul. 2018, doi: 10.1002/jmri.25932.

[94] H. El Aidi *et al.*, “Cardiac magnetic resonance imaging findings and the risk of cardiovascular events in patients with recent myocardial infarction or suspected or known coronary artery disease: a systematic review of prognostic studies,” *J. Am. Coll. Cardiol.*, vol. 63, no. 11, pp. 1031–1045, Mar. 2014, doi: 10.1016/j.jacc.2013.11.048.

[95] B. Ambale-Venkatesh *et al.*, “Cardiovascular Event Prediction by Machine Learning: The Multi-Ethnic Study of Atherosclerosis,” *Circ. Res.*, vol. 121, no. 9, pp. 1092–1101, Oct. 2017, doi: 10.1161/CIRCRESAHA.117.311312.

[96] I. H. Sarker, “Machine Learning: Algorithms, Real-World Applications and Research Directions,” *SN Comput. Sci.*, vol. 2, no. 3, p. 160, Mar. 2021, doi: 10.1007/s42979-021-00592-x.

[97] “Foundations of Machine Learning,” MIT Press. Accessed: Mar. 29, 2024. [Online]. Available: https://mitpress.mit.edu/9780262039406/foundations-of-machine-learning/

[98] S. S. Yadav and S. M. Jadhav, “Deep convolutional neural network based medical image classification for disease diagnosis,” *J. Big Data*, vol. 6, no. 1, p. 113, Dec. 2019, doi: 10.1186/s40537-019-0276-2.

[99] M. W. Wagner, K. Namdar, A. Biswas, S. Monah, F. Khalvati, and B. B. Ertl-Wagner, “Radiomics, machine learning, and artificial intelligence—what the neuroradiologist needs to know,” *Neuroradiology*, vol. 63, no. 12, pp. 1957–1967, 2021, doi: 10.1007/s00234-021-02813-9.

[100] S. Raschka, “Model Evaluation, Model Selection, and Algorithm Selection in Machine Learning,” Nov. 10, 2020, *arXiv*: arXiv:1811.12808. doi: 10.48550/arXiv.1811.12808.

[101] L. Breiman, “Random Forests,” *Mach. Learn.*, vol. 45, no. 1, pp. 5–32, Oct. 2001, doi: 10.1023/A:1010933404324.

[102] J. R. Quinlan, “Induction of decision trees,” *Mach. Learn.*, vol. 1, no. 1, pp. 81–106, Mar. 1986, doi: 10.1007/BF00116251.

[103] I. Guyon and A. Elisseeff, “An Introduction to Variable and Feature Selection,” *J. Mach. Learn. Res.*, vol. 3, no. Mar, pp. 1157–1182, 2003.

[104] W. Zhang, Y. Guo, and Q. Jin, “Radiomics and Its Feature Selection: A Review,” *Symmetry*, vol. 15, no. 10, Art. no. 10, Oct. 2023, doi: 10.3390/sym15101834.

[105] M. B. Kursa and W. R. Rudnicki, “Feature Selection with the Boruta Package,” *J. Stat. Softw.*, vol. 36, pp. 1–13, Sep. 2010, doi: 10.18637/jss.v036.i11.

[106] E. J. Benjamin *et al.*, “Heart Disease and Stroke Statistics-2019 Update: A Report From the American Heart Association,” *Circulation*, vol. 139, no. 10, pp. e56–e528, Mar. 2019, doi: 10.1161/CIR.0000000000000659.

[107] C. M. Wacker, A. W. Hartlep, S. Pfleger, L. R. Schad, G. Ertl, and W. R. Bauer, “Susceptibility-sensitive magnetic resonance imaging detects human myocardium supplied by a stenotic coronary artery without a contrast agent,” *J. Am. Coll. Cardiol.*, vol. 41, no. 5, pp. 834–840, Mar. 2003, doi: 10.1016/s0735-1097(02)02931-5.

[108] P. Bernhardt *et al.*, “Blood oxygen level-dependent magnetic resonance imaging using T2-prepared steady-state free-precession imaging in comparison to contrast-enhanced myocardial perfusion imaging,” *Int. J. Cardiol.*, vol. 147, no. 3, pp. 416–419, Mar. 2011, doi: 10.1016/j.ijcard.2009.09.547.

[109] R. Manka, I. Paetsch, B. Schnackenburg, R. Gebker, E. Fleck, and C. Jahnke, “BOLD cardiovascular magnetic resonance at 3.0 tesla in myocardial ischemia,” *J. Cardiovasc. Magn. Reson. Off. J. Soc. Cardiovasc. Magn. Reson.*, vol. 12, no. 1, p. 54, Sep. 2010, doi: 10.1186/1532-429X-12-54.

[110] T. D. Karamitsos *et al.*, “Relationship between regional myocardial oxygenation and perfusion in patients with coronary artery disease: insights from cardiovascular magnetic resonance and positron emission tomography,” *Circ. Cardiovasc. Imaging*, vol. 3, no. 1, pp. 32–40, Jan. 2010, doi: 10.1161/CIRCIMAGING.109.860148.

[111] J. R. Arnold *et al.*, “Myocardial oxygenation in coronary artery disease: insights from blood oxygen level-dependent magnetic resonance imaging at 3 tesla,” *J. Am. Coll. Cardiol.*, vol. 59, no. 22, pp. 1954–1964, May 2012, doi: 10.1016/j.jacc.2012.01.055.

[112] C. Jahnke, R. Gebker, R. Manka, B. Schnackenburg, E. Fleck, and I. Paetsch, “Navigator-gated 3D blood oxygen level-dependent CMR at 3.0-T for detection of stress-induced myocardial ischemic reactions,” *JACC Cardiovasc. Imaging*, vol. 3, no. 4, pp. 375–384, Apr. 2010, doi: 10.1016/j.jcmg.2009.12.008.

[113] T. Walcher, R. Manzke, V. Hombach, W. Rottbauer, J. Wöhrle, and P. Bernhardt, “Myocardial perfusion reserve assessed by T2-prepared steady-state free precession blood oxygen level-dependent magnetic resonance imaging in comparison to fractional flow reserve,” *Circ. Cardiovasc. Imaging*, vol. 5, no. 5, pp. 580–586, Sep. 2012, doi: 10.1161/CIRCIMAGING.111.971507.

[114] B. Baessler *et al.*, “Cardiac MRI and Texture Analysis of Myocardial T1 and T2 Maps in Myocarditis with Acute versus Chronic Symptoms of Heart Failure,” *Radiology*, vol. 292, no. 3, pp. 608–617, Sep. 2019, doi: 10.1148/radiol.2019190101.

[115] S. Lundberg and S.-I. Lee, “A Unified Approach to Interpreting Model Predictions,” Nov. 24, 2017, *arXiv*: arXiv:1705.07874. doi: 10.48550/arXiv.1705.07874.

[116] G. Femia, J. K. French, C. Juergens, D. Leung, and S. Lo, “Right ventricular myocardial infarction: pathophysiology, clinical implications and management,” *Rev. Cardiovasc. Med.*, vol. 22, no. 4, Art. no. 4, Dec. 2021, doi: 10.31083/j.rcm2204131.

[117] A. Larroza, A. Materka, M. P. López-Lereu, J. V. Monmeneu, V. Bodí, and D. Moratal, “Differentiation between acute and chronic myocardial infarction by means of texture analysis of late gadolinium enhancement and cine cardiac magnetic resonance imaging,” *Eur. J. Radiol.*, vol. 92, pp. 78–83, Jul. 2017, doi: 10.1016/j.ejrad.2017.04.024.

[118] J. E. Park, S. Y. Park, H. J. Kim, and H. S. Kim, “Reproducibility and Generalizability in Radiomics Modeling: Possible Strategies in Radiologic and Statistical Perspectives,” *Korean J. Radiol.*, vol. 20, no. 7, p. 1124, Jul. 2019, doi: 10.3348/kjr.2018.0070.

[119] S. Schalla *et al.*, “Right ventricular function in dilated cardiomyopathy and ischemic heart disease: assessment with non-invasive imaging,” *Neth. Heart J. Mon. J. Neth. Soc. Cardiol. Neth. Heart Found.*, vol. 23, no. 4, pp. 232–240, Apr. 2015, doi: 10.1007/s12471-015-0673-x.

[120] “Cine MRI-Derived Radiomics Features of the Cardiac Blood Pool: Periodicity, Specificity, and Reproducibility - Lin - 2023 - Journal of Magnetic Resonance Imaging - Wiley Online Library.” Accessed: Apr. 02, 2024. [Online]. Available: https://onlinelibrary.wiley.com/doi/abs/10.1002/jmri.28572

[121] M. Chen, X. Shi, Y. Zhang, D. Wu, and M. Guizani, “Deep Feature Learning for Medical Image Analysis with Convolutional Autoencoder Neural Network,” *IEEE Trans. Big Data*, vol. PP, pp. 1–1, Jun. 2017, doi: 10.1109/TBDATA.2017.2717439.

[122] “https://pyradiomics.readthedocs.io/en/latest/features.html.”

Declarations

Conflicts of Interest:

NM reports no conflicts of interest.

MGF is an external consultant to Circle Cardiovascular Imaging Inc and co-founder of Area19 Medical Inc. and shareholder of AiVALON Technologies. Inc. MGF is listed as a holder of: United States Patent No. 14/419,877: Inducing and measuring myocardial oxygenation changes as a marker for heart disease; United States Patent No. 15/483,712: Measuring oxygenation changes in tissue as a marker for vascular function; United States Patent No 10,653,394: Measuring oxygenation changes in tissue as a marker for vascular function - continuation; Canadian Patent CA2020/051776: Method and apparatus for determining biomarkers of vascular function utilizing bold CMR images. MGF is shareholder and advisor of Circle Cardiovascular Imaging Inc., Area19 Medical Inc., and AiVALON Technologies.

MB is the Officer and shareholder of Area 19 Medical Inc.